Featured in Physics

Improved Electron-Nuclear Quantum Gates for Spin Sensing and Control

H.B. van Ommen,[1,2,†] G.L. van de Stolpe,[1,2,†] N. Demetriou,[1,2] H.K.C. Beukers,[1,2] J. Yun,[1,2] T.R.J. Fortuin,[1,2] M. Iuliano,[1,2] A.R.-P. Montblanch,[1,2] R. Hanson,[1,2] and T.H. Taminiau[1,2,*]

[1] *QuTech, Delft University of Technology, P.O. Box 5046, 2600 GA Delft, The Netherlands*

[2] *Kavli Institute of Nanoscience Delft, Delft University of Technology, P.O. Box 5046, 2600 GA Delft, The Netherlands*

(Received 5 November 2024; revised 6 February 2025; accepted 10 February 2025; published 11 April 2025)

The ability to sense and control nuclear spins near solid-state defects might enable a range of quantum technologies. Dynamically decoupled radio-frequency (DDrf) control offers a high degree of design flexibility and long electron-spin coherence times. However, previous studies have considered simplified models and little is known about optimal gate design and fundamental limits. Here, we develop a generalized DDrf framework that has important implications for spin sensing and control. Our analytical model, which we corroborate by experiments on a single NV center in diamond, reveals the mechanisms that govern the selectivity of gates and their effective Rabi frequencies, and enables flexible detuned gate designs. We apply these insights to numerically show a 60× sensitivity enhancement for detecting weakly coupled spins and study the optimization of quantum gates in multiqubit registers. These results advance the understanding for a broad class of gates and provide a toolbox for application-specific design, enabling improved quantum control and sensing.

DOI: 10.1103/PRXQuantum.6.020309

I. INTRODUCTION

Sensing and controlling nuclear spins in the vicinity of optically active solid-state defects, such as the nitrogen-vacancy (NV) center in diamond, has opened up various opportunities in the fields of quantum sensing and quantum information processing [1–4]. Sensing nuclear spins outside the host crystal might bring chemical structure determination to the single-molecule level [1,3,5,6]. More strongly coupled nuclear spins inside the host material can be used for quantum information processing, for which advances in the number of available qubits [7], in gate fidelities [8,9], and in the possibility of connecting systems via an optical interface [2,10] have led to proof-of-principle demonstrations of increasing complexity [3,4,11].

Central to these developments has been the ability to sense and control nuclear spins using the electron spin of the defect through the hyperfine interaction [12–17]. In particular, dynamical-decoupling (DD) protocols have been used to detect nuclear-magnetic-resonance signals [18,19] and allow for selective universal nuclear-spin control [20]. Compared to traditional DD sensing, the recently developed DDrf sequence [14], which combines DD with radio-frequency (rf) pulses, unlocks additional sensing and control directions [Fig. 1(a)] and offers increased flexibility for gate optimization [9]. These advantages have helped to enable the sensing of large nuclear-spin clusters [3,7], extend the number of nuclear spins available to defect centers for information processing [14,21,22], and realize high two-qubit gate fidelities (> 99.9%) [9].

In this work, we introduce a generalized version of the DDrf framework, enhancing the performance of the sequence for nuclear sensing and control, as well as revealing important limitations on sensitivity and selectivity. We derive analytical expressions that give a more complete description of the electron-nuclear dynamics compared to previous work [14] and verify their predictions experimentally using a single NV center and its surrounding ^{13}C nuclear spins. Based on these insights, we modify the DDrf sequence to optimize the effective electron-nuclear interaction strength and mitigate crosstalk of quantum gates. These results have applications in the field of nano-NMR [1,3,6] and provide a comprehensive toolbox for designing quantum gates in multiqubit electron-nuclear-spin systems [14,21].

*Contact author: t.h.taminiau@tudelft.nl

†These authors contributed equally to this work.

Published by the American Physical Society under the terms of the Creative Commons Attribution 4.0 International license. Further distribution of this work must maintain attribution to the author(s) and the published article's title, journal citation, and DOI.

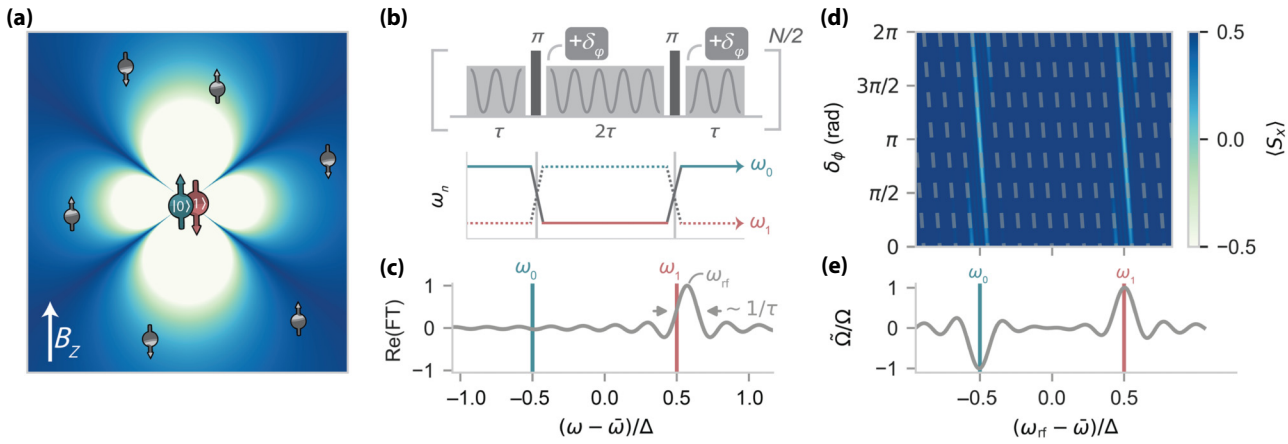

FIG. 1. The DDrf framework. (a) A schematic of the system considered here, comprising a single electron spin (the red and blue colors denote the spin state), surrounded by a nonuniform distribution of nuclear spins (gray). The background brightness corresponds to the hyperfine ($A_\parallel$) frequency shift Δ induced by the electron spin. B_z is the external magnetic field. (b) The DDrf sequence, where rf driving (with phase updates δ_ϕ) of the nuclear spin (gray) is interleaved with decoupling pulses on the electron spin (black). The bottom row indicates the precession frequency of the nuclear spin (ω_n), for initial electron-spin state $|0\rangle$ (solid line) or $|1\rangle$ state (dotted line). The total sequence time is $T = 2N\tau$. (c) A schematic showing the Fourier transform (FT) of a single rf pulse applied at frequency $\omega_{rf} = \omega_1 + \Delta_1$. The bandwidth of the pulse is inversely proportional to the pulse length ($\propto 1/(2\tau)$). (d) A simulation of nuclear-spin spectroscopy, where the electron spin (starting in $(|0\rangle + |1\rangle)/\sqrt{2}$) is used to sense an unpolarized nuclear spin by applying the DDrf sequence of (b). The brighter colors indicate a drop in electron coherence ($\langle S_x \rangle$), observed when δ_ϕ matches Eq. (3) (dashed gray line). (e) The effective nuclear-spin Rabi frequency $\tilde{\Omega}$ [Eq. (5)] of the DDrf sequence, as a fraction of the bare Rabi frequency Ω, when following the phase increment δ_ϕ [Eq. (3), dashed line in (d)]. A significant electron-nuclear interaction is possible over a range of rf frequencies ($\omega_{rf} \neq \omega_1$), albeit with a lower effective interaction strength $\tilde{\Omega}$.

II. DECOHERENCE-PROTECTED RADIO-FREQUENCY QUANTUM GATES

We first describe the DDrf gates. Compared to the original description [14], we present a generalized framework, explicitly including the off-resonant driving of nuclear-spin transitions. We will show that this refinement has important implications for the performance of quantum gates and sensing sequences implemented with DDrf control.

We consider an electronic spin interacting with a number of nuclear spins via a hyperfine interaction [see Fig. 1(a)]. To retain generality for defects with different spin numbers [23–27], we assume that two electron spin states are selected to use as a qubit and describe these as a pseudo-spin-$\frac{1}{2}$ system spanned by $|0\rangle$ and $|1\rangle$.

The main challenge for electron-nuclear gates in such systems is that the electron interacts with all nuclear spins, as well as other noise sources, leading to decoherence and crosstalk [13,14,28]. Hence, a well-designed electron-nuclear two-qubit gate or sensing sequence aims to realize a conditional interaction with a selected (group of) target spin(s), while protecting electron coherence by decoupling all other interactions and noise sources.

The DDrf gate consists of a sequence of DD pulses on the electron spin, interleaved with rf pulses that drive the nuclear-spin transitions, as illustrated in Fig. 1(b). We consider sequences of the form $(\tau - \pi - 2\tau - \pi - \tau)^{N/2}$, where N is the number of π pulses and 2τ is the interpulse delay. The DD sequence aims to decouple the electron spin from the surrounding spins and magnetic field fluctuations, extending the electron-spin coherence [15]. The interleaved rf pulses aim to manipulate selected nuclear spins and to recouple them to the electron spin [14].

In the frame of the electron energy splitting, the Hamiltonian for the electron spin and a single nuclear spin is [14] (Appendix B)

$$H = \bar{\omega} I_z + \Delta S_z I_z, \tag{1}$$

where $\bar{\omega} = (\omega_0 + \omega_1)/2$ is the mean nuclear-spin frequency, with ω_0 and ω_1 as the nuclear-spin precession frequencies for electron-spin states $|0\rangle$ or $|1\rangle$, respectively. $\Delta = \omega_0 - \omega_1$ is set by the strength of the electron-nuclear hyperfine interaction [12] (see Appendix B). S_z and I_z are the electronic and nuclear spin-$\frac{1}{2}$ operators, respectively. Note that we neglect the anisotropy of the hyperfine interaction (terms such as $A_\perp S_z I_x$). While this interaction can create complex dynamics and can be used for qubit control [12,20], the effects can typically be minimized by applying strong magnetic fields ($\omega_L \gg A_\perp, A_\parallel$) and setting the interpulse delay τ to a multiple of the nuclear-spin Larmor period $\tau_L = 2\pi/\omega_L$ [14].

The rf pulses selectively drive nuclear spins, recoupling them to the electron-spin. In the interaction picture, the

Hamiltonian during the rf pulses for a single nuclear spin is (in the rotating frame at the rf frequency $\omega_{\rm rf}$) as follows:

$$H_{\rm rf} = |0\rangle\langle 0| \otimes \Delta_0 I_z + |1\rangle\langle 1| \otimes \Delta_1 I_z + \mathbb{I} \otimes \Omega(\cos\phi I_x + \sin\phi I_y), \quad (2)$$

where $\Delta_0 = \omega_{\rm rf} - \omega_0$ and $\Delta_1 = \omega_{\rm rf} - \omega_1$ are the detunings between the nuclear-spin transition frequencies and the rf frequency, ϕ is the phase, and Ω is the Rabi frequency of the (bare) rf drive.

Because the frequencies Δ_0 and Δ_1 differ by Δ, an rf pulse will generally cause a different nuclear-spin evolution for the $|0\rangle$ and $|1\rangle$ electron states, enabling the construction of conditional two-qubit gates. Similarly, other spins with $\Delta_0', \Delta_1' \neq \Delta_0, \Delta_1$ undergo a different evolution, introducing an element of selectivity between different nuclear spins. Previous work [14] has assumed that resonant rf driving ($\Delta_1 = 0$) combined with $\Delta_0 \gg \Omega$ results in negligible driving during the electron $|0\rangle$ state, thus neglecting that part of the driving term in $H_{\rm rf}$. Below, we show that this term cannot generally be neglected, due to the broad effective bandwidth of the short rf pulses (small τ) in the DDrf sequence.

To ensure that the DDrf sequence generates the desired gate, the phase of each rf pulse must be set so that the pulses result in a constructive build-up of rotations on the nuclear spin. This equates to following the phase evolution of the nuclear spin in the frame of the rf frequency. In the decoupling sequence, this is achieved by incrementing the phase of the next rf pulse by a phase-angle δ_ϕ every time a decoupling π pulse is applied on the electron spin [Fig. 1(b)].

In one DDrf block ($N = 2$), the nuclear spin accumulates a total phase of $2\Delta_0\tau + 2\Delta_1\tau$ (up to a correction for the ac Stark shift; see Appendix D). By adding a π phase shift with each decoupling pulse, the direction of the rf drive is inverted synchronous to the flipping of the electron spin state, creating a conditional electron-nuclear interaction. This gives rise to a resonance condition, satisfied by setting a single-pulse phase increment:

$$\delta_\phi = -(\Delta_0 + \Delta_1)\tau + \pi, \quad (3)$$

up to multiples of 2π. The dependence of the mean precession frequency during the gate, $(\Delta_0 + \Delta_1)/2$, on the electron-nuclear hyperfine interaction means that this resonance condition provides an additional mechanism for selectivity between different nuclear spins. Importantly, Eq. (3) constitutes a generalization of the phase-increment resonance considered in previous work (restricted to $\Delta_1 = 0, \Delta_0 = \Delta$) [14].

To quantify the strength of the conditional interaction, we evaluate the unitary of the total DDrf sequence under the Hamiltonian in Eq. (2), setting the phase increment to Eq. (3). We assume that the rotation due to an individual rf pulse is small ($\Omega\tau \ll 1$), which is typical for DDrf gates, because the total rotation angle of the gate is broken up into N pieces. In this limit, the evolution can be described by a conditional rotation $V_{\rm CROT}$ of the nuclear spin (Appendix K):

$$V_{\rm CROT} = |0\rangle\langle 0| \otimes R_x(N\tilde{\Omega}\tau) + |1\rangle\langle 1| \otimes R_x(-N\tilde{\Omega}\tau), \quad (4)$$

with an *effective* Rabi frequency given by

$$\tilde{\Omega} = \Omega\left(\mathrm{sinc}(\Delta_1\tau) - \mathrm{sinc}(\Delta_0\tau)\right), \quad (5)$$

where $R_x(\theta) = e^{-i\theta I_x}$, with the x axis set by the phase of the first rf pulse and the sinc function is defined as $\mathrm{sinc}(x) = \sin(x)/x$. Note that previous work has neglected off-resonant driving, setting $\Delta_0\tau \gg 1$ and $\Delta_1 = 0$, so that Eq. (5) reduces to $\tilde{\Omega} = \Omega$ [14].

Setting $\tilde{\Omega}N\tau = \pi/2$ in Eq. (4) results in a fully entangling gate, equivalent to a controlled-NOT (CNOT) up to single-qubit rotations. Furthermore, Eq. (5) shows that such a gate can be constructed in the neighborhood of the ω_0 and ω_1 frequencies, over a bandwidth given by approximately $1/\tau$ [see Figs. 1(c)–1(e)]. Note that this can be understood as the result of evaluating the Fourier transform of an individual rf pulse (applied at $\omega_{\rm rf}$) at the nuclear-spin transitions ω_0 and ω_1 and that the bandwidth is much larger than would be expected from power broadening due to Ω.

In the following sections, we first experimentally verify Eqs. (3) and (5) by performing DDrf spectroscopy on a single NV center in diamond (Sec. III). Then, we investigate the weak-coupling regime ($\Delta\tau \lesssim \pi$), for which Eq. (5) poses an inherent trade-off between the effective interaction strength and the degree of electron decoherence (Sec. IV). Finally, we apply these findings to two applications: sensing a single nuclear spin (Sec. V) and qubit control in a realistic nuclear-spin quantum register (Secs. VI and VII).

III. GENERALIZED DDrf SPECTROSCOPY

Even though all results in this work can be generalized to other electron-nuclear-spin systems, in the following we will consider in particular the $m_s = \{0, -1\}$ electron-spin subspace of the NV center in diamond ($S = 1$) and its surrounding ^{13}C nuclear spins. The main difference compared with other electron spin systems is how Δ_0 and Δ_1 depend on the hyperfine coupling. See Beukers *et al.* [29] for experiments and simulation on an electron-spin-1/2 system (the tin-vacancy center in diamond), for which the dependence of $\Delta_0 + \Delta_1$ vanishes up to second-order corrections due to the perpendicular hyperfine component $A_\perp$ [20,30,31].

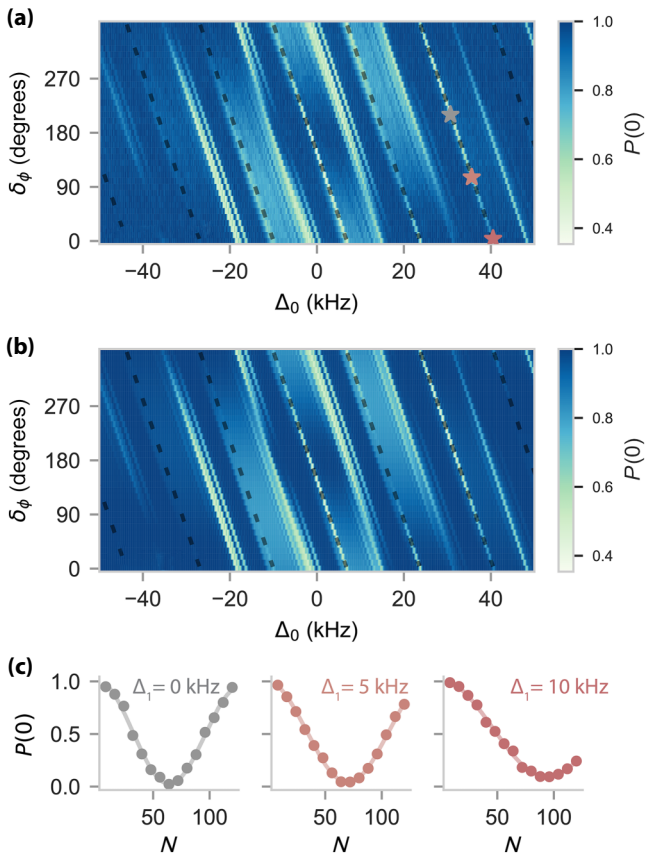

FIG. 2. Generalized DDrf spectroscopy. (a) Experimental data showing DDrf spectroscopy on the nuclear-spin environment of an NV center, sweeping the rf frequency $\Delta_0 = \omega_{\rm rf} - \omega_0$ and the phase update δ_ϕ ($\tau = 29.632\,\mu$s, $N = 24$, $\Omega = 356$ Hz). Single nuclear spins show up as descending diagonal lines following their frequency-phase resonance [Eq. (3)], while the bath of weakly coupled spins shows up as a band. The dashed black line indicates the resonance condition of a single spin (C_0, $\Delta = -30.7$ kHz). The colored stars correspond to the parameters used for the data in (c). $P(0)$ corresponds to the remaining electron-spin coherence (see Appendix A). (b) Simulation: a numerical calculation of the DDrf spectroscopy signal using the hyperfine couplings of 15 individual nuclear spins and a statistical distribution for weakly coupled (bath) spins with $|\Delta| < 6$ kHz (see Appendix C). (c) An experimental demonstration of two-qubit gates with a detuned rf field ($N = 32, \Omega = 313$ Hz, $\Delta_1 = 5, 10$ kHz, $\tau = 24.654\,\mu$s), showing lower effective Rabi frequencies compared to resonant driving (gray data, $\Delta_1 = 0$ kHz).

All experimental results are obtained from a single NV center in a natural-abundance (1.1%) ^{13}C diamond sample at cryogenic temperatures (4 K), with a $B_z = 189.1$ mT magnetic field along the NV symmetry axis (Appendix A). At this field, the nuclear quantization axes are approximately parallel to the z axis and $A_\perp$ only contributes as a frequency shift (see Appendix B).

To verify Eqs. (3) and (5) experimentally, we perform nuclear-spin spectroscopy using DDrf, by varying both the rf frequency and single-pulse phase increment δ_ϕ [Fig. 2(a), similar to Fig. 1(d)]. First, the electron spin is initialized in a superposition. A drop in the measured electron coherence after application of the DDrf gate indicates interaction between the electron spin and one or more nuclear spins.

We observe a number of traces that all follow the predicted resonance condition [Eq. (3)]. The spectrum shows isolated traces indicating interactions with single nuclear spins and a broad bandlike feature corresponding to a bath of weakly coupled spins. The measured data are well recreated by a numerical simulation modeling 15 individual spins (see Table I), together with a statistically distributed spin bath of many weakly coupled spins [Fig. 2(b); for simulation details, see Appendix C].

Next, we show that the phase-increment condition [Eq. (3)], together with the single-pulse bandwidth, enables the construction of electron-nuclear gates even if the rf driving frequency is far off resonance ($\Delta_1 \gg \Omega$). We perform such detuned gates on a single nuclear spin and compare them to an on-resonant gate applied to the same spin [Fig. 2(c)]. All gates achieve near-unity contrast (up to some decay due to experimental noise), though the detuned version yields a reduced gate speed, as predicted by Eq. (5). We further confirm the entangling nature of detuned gates by evaluating the process matrix obtained from numerical simulations (see Appendix D).

The discussion in this section shows that nuclear-spin resonance conditions are set by both the rf frequency and the single-pulse phase increment. Furthermore, quantum gates can be constructed even with significantly detuned driving frequencies by properly updating the pulse phases. This insight expands the parameter space from which gates and sensing sequences can be constructed, yielding additional possibilities for optimization.

IV. WEAK-COUPLING REGIME ($\Delta\tau \lesssim \pi$)

When the bandwidth related to the rf pulses (approximately $1/\tau$) is larger than, or on the same order as, the hyperfine splitting Δ, it is no longer valid to assume driving of only one of the nuclear-spin transitions ω_1 and ω_0 [Fig. 3(a), Eq. (2)]. In this readily encountered regime, rotations for the electron $|0\rangle$ state can cancel (or add to) the rotations for the electron $|1\rangle$ state, reducing (or enhancing) the effective rotation.

We first consider the conditional gate [Eq. (4)], for which the π phase shift in δ_ϕ inverts the rf rotation axis between subsequent pulses. In the limit of small $\Delta\tau$, $\tilde{\Omega}$ is strongly attenuated [Eq. (5)], proportional to $(\Delta\tau)^{-2}$ for on-resonance addressing ($\Delta_1 = 0$) and proportional to $(\Delta\tau)^{-1}$ for the optimal driving condition discussed in Sec. V [see Fig. 4(b)]. Additionally, the extrema of $\tilde{\Omega}$ shift away from the ω_1, ω_0 transitions [Fig. 3(b) and Eq. (9)]. This explains why the spectroscopy signals of weakly

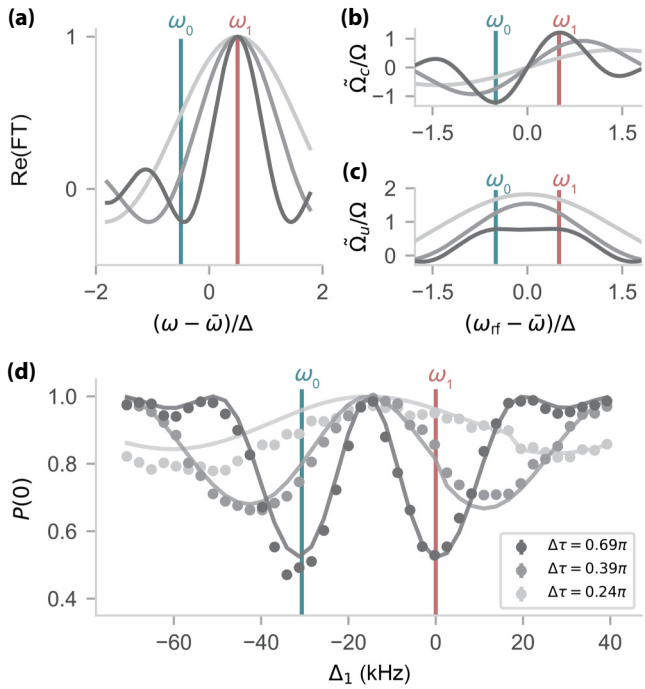

FIG. 3. The weak-coupling regime. (a) A schematic showing the Fourier transform of a single rf pulse [as in Fig. 1(c)] applied at $\omega_{rf} = \omega_1$, for $\Delta\tau \lesssim \pi$. As τ decreases, the pulse bandwidth increases, leading to the addressing of both the ω_1 and ω_0 transitions. (b) The effective Rabi frequency $\tilde{\Omega}_c$ for a conditional gate (as a function of ω_{rf}) is enhanced or suppressed when both transitions are addressed [Eq. (5)]. (c) The same as in (b) but for an unconditional gate [Eq. (7)]. (d) Experimental spectroscopy data as in Fig. 2(a) confirming the effective Rabi frequency for conditional gates for various $\Delta\tau$ (fixing the gate time $2N\tau \approx 1.4$ ms, $\Omega = 313$ Hz). Here, δ_ϕ is set to track the phase-increment resonance condition of a single nuclear spin [$C_0, \Delta = -30.7$ kHz, dashed black line in Fig. 2(a)]. A shorter τ leads to a contrast reduction and a shift of the optimal rf frequency. The analytical prediction (solid gray lines), using no free parameters, is calculated using $P(0) = 1/2\,(1 + \cos 2\tilde{\Omega}N\tau)$, with $\tilde{\Omega}$ taken from (b). We attribute the model-data discrepancy to the specifics of the rf pulse envelope shape and variable rf transmission, which have not been taken into account (Appendix A).

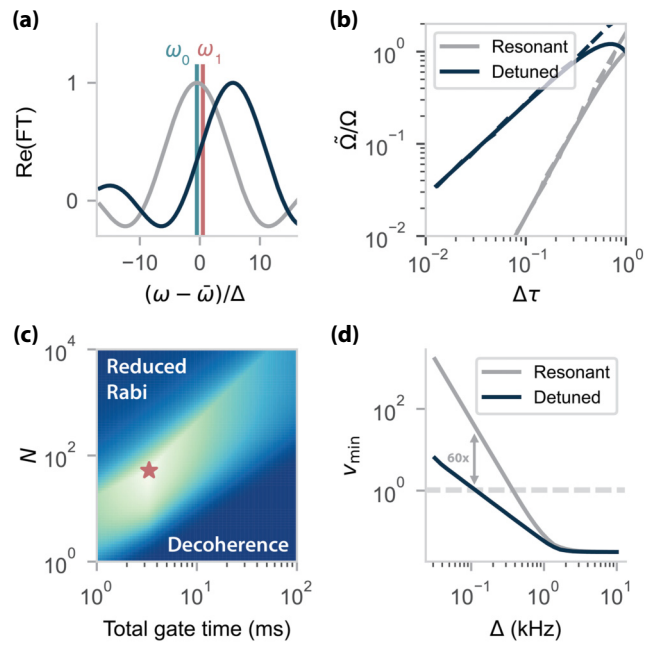

FIG. 4. The optimized detuned sensing. (a) A schematic illustrating the maximum DDrf contrast if the ω_0 and ω_1 transitions are on the slope of the rf pulse envelope. (b) Numerical calculation of the Rabi frequency suppression as a function of $\Delta\tau$ for $\Delta < \tau$. When driving on resonance, $\tilde{\Omega} \propto (\Delta\tau)^2$; however, by using the optimal detuning [Eq. (9)], $\tilde{\Omega} \propto \Delta\tau$ (scaling indicated by dashed lines). The effective Rabi frequency can thus be much improved when purposefully driving off resonance. (c) The inverse sensitivity (v_{min}^{-1}), varying the number of pulses N and the total sequence time t. Short interpulse spacing τ (corresponding to short t and high N) leads to the driving of both transitions, while a long τ (i.e., using low N) leads to electron decoherence. The red star denotes the optimal parameters. (d) Detuned sensing achieves orders of magnitude higher sensitivity, still allowing for single-spin sensitivity (dotted gray line) for small Δ.

coupled spins ($\Delta \ll 1/\tau$) are suppressed and appear at detuned frequencies [broad features in Fig. 2(a)].

This analysis reveals an inherent trade-off present in DDrf gates. While a short interpulse delay τ improves the coherence of the electron spin [15], it also reduces the effective Rabi frequency, thereby increasing the total gate duration $T = \pi/\tilde{\Omega}$ required for a $\pm\pi/2$ gate or requiring an increase in Ω.

We experimentally validate Eq. (5) by driving nuclear spin C_0 at different rf frequencies, while updating the rf phases according to Eq. (3) [Fig. 3(d)]. This amounts to tracking the nuclear-resonance condition apparent in Fig. 2(a). Such a measurement directly yields the spectral signature of the reduced Rabi frequency, which is in good agreement with Eq. (5).

We repeat this measurement for different rf pulse durations τ, keeping the rf amplitude ($\Omega = 313$ Hz at ω_1) and the total DDrf driving time (approximately 1.4 ms) fixed using N. For shorter τ, a decrease in signal contrast and a shift of the optimal rf frequency can be observed, as predicted by Eq. (5).

The DDrf gate can also be used to perform an unconditional rotation of the nuclear spin, by leaving out the π phase shift from δ_ϕ [Eq. (3)] [14]. The DDrf gate unitary then becomes

$$V_{ROT} = \mathbb{I} \otimes R_x(N\Omega_u\tau), \tag{6}$$

with effective (unconditional) Rabi frequency

$$\tilde{\Omega}_u = \Omega\,(\mathrm{sinc}(\Delta_1\tau) + \mathrm{sinc}(\Delta_0\tau))\,. \tag{7}$$

In contrast to the conditional case, $\tilde{\Omega}_u$ is enhanced at small $\Delta\tau$ [Fig. 3(c)], as without the extra π phase shift, the rf rotations build up constructively. In the limit $\Delta \ll 1/(2\tau)$, the effective Rabi frequency Ω_u approaches 2Ω, identical to constant rf driving of a nuclear-spin transition while keeping the electron spin in an eigenstate.

We identify three approaches for mitigating the reduced Rabi frequency for conditional gates. First, for a fixed gate length $2N\tau$, the number of decoupling pulses N can be traded for the rf pulse length (approximately 2τ), shrinking the pulse bandwidth to avoid driving both transitions. This comes at the cost of decreasing the effectiveness of the electron decoupling, as longer interpulse delays protect less effectively against low-frequency noise [15]. Second, given a certain pulse length, the rf frequency can be detuned to maximize Eq. (5). Third, one could increase the physical rf amplitude to compensate for the reduced Rabi frequency, although this poses experimental challenges, and our model validity is constrained to $\Omega\tau \ll 1$. In the following sections, we explore these approaches in more detail, in the context of nuclear-spin sensing and multiqubit control.

V. OPTIMAL SENSITIVITY FOR SENSING A SINGLE NUCLEAR SPIN

To highlight the practical significance of the presented insights, we demonstrate how to optimize the DDrf sequence for sensing a single weakly coupled nuclear spin (with hyperfine coupling Δ). For example, this nuclear spin could be a single proton or ^{13}C spin, potentially outside of the host crystal [32]. The goal is to minimize the (single-spin) sensitivity, defined as [33] (Appendix E)

$$v_{\min} = \frac{2\pi e^{\chi(N,t)}}{\tilde{\Omega}_{\max}(\Delta, N, t)\sqrt{t}}, \tag{8}$$

where $\chi(N,t)$ is the sensor decoherence function (here taken from the experimental observations of Ref. [15]), $\tilde{\Omega}_{\max}$ is the maximum attainable effective Rabi frequency (given Δ and N), and $t = 2N\tau$ is the single-experiment sensing time [33]. For simplicity, we assume unity readout contrast and zero sensor overhead (Appendix E).

The expression for $v_{\min}$ in Eq. (8) conveys the minimum number of nuclear spins required that together yield a detectable signal in 1 s of integration time. Evidently, to achieve single-spin sensitivity ($v_{\min} < 1$), the *effective* Rabi frequency $\tilde{\Omega}$, which sets the effective coupling to the signal, should be as large as possible, while retaining sufficient electron coherence ($e^{-\chi(N,t)}$). The choice of N presents us with an inherent trade-off between these two factors. Generally, larger N (shorter τ values) increases the electron coherence, but decreases $\tilde{\Omega}_{\max}$ (see Sec. IV). However, optimizing over the large parameter space is challenging.

We first reduce the parameter-space size by calculating the rf detuning that maximizes $\tilde{\Omega}$. For $\Delta \gtrsim 2\pi/\tau$, the rf driving when the electron is in the $|0\rangle$ state can be neglected and the optimal effective Rabi frequency is always attained when driving on resonance ($\Delta_1 = 0$). However, when $\Delta \lesssim 2\pi/\tau$, significant enhancement is possible by detuning the rf frequency. We find that the optimum setting for Δ_1 is (approximately) given by (Appendix F)

$$\Delta_1 = \begin{cases} -\dfrac{w_s}{\tau} + \Delta/2, & \text{if } \tau \lesssim 2\pi/|\Delta|, \\ 0, & \text{otherwise}, \end{cases} \tag{9}$$

where $w_s \approx 2.082$ is the first root of the second derivative of the sinc function. Conceptually, this condition is satisfied when the detuning is such that the gradient of the rf pulse envelope is maximal in between the ω_0 and ω_1 transitions [Fig. 4(a)]. While for $\Delta_1 = 0$, $\tilde{\Omega} \propto (\Delta\tau)^2$, using the optimum Δ_1 changes the scaling to $\tilde{\Omega} \propto \Delta\tau$ [Fig. 4(b)]. We verify that Eq. (9) maximizes Eq. (5) in the small-Δ regime (Appendix F).

Next, we evaluate the optimal rf amplitude. For the situation of a very weakly coupled spin, the reduced Rabi frequency can be partially compensated for by increasing the physical rf amplitude Ω. However, simply setting the rf amplitude to the inverse of $\tilde{\Omega}/\Omega$ leads to unrealistically high values when $\tau \ll 2\pi/\Delta$. Moreover, our model of the effective Rabi frequency strictly only holds for $\Omega\tau \ll 1$. Therefore, in the current analysis, we set an upper bound for the rf amplitude: $\Omega < 1/(2\tau)$. Additionally, we limit the maximum value to $\Omega < 10\,\text{kHz}$, as higher Rabi frequencies are typically challenging to reach without specialized rf transmitters, especially at cryogenic temperatures [34,35].

Then, to find the optimal sensing parameters, we evaluate (the inverse of) Eq. (8), sweeping the number of pulses N and total sequence time $t = 2N\tau$, while continuously updating the rf detuning and rf amplitude to maximize $\tilde{\Omega}$ [Fig. 4(c) and Appendix G]. As expected, there exists an optimal regime that balances the expected reduction in Rabi frequency and electron decoherence [bright sliver in Fig. 4(c)]. We compare the sensitivity of the (conventional) resonant gate with the detuned protocol by extracting the optimal value for various Δ [Fig. 4(d)] and find that the latter outperforms the former for small Δ. A divergence between the two can be observed at $\Delta/(2\pi) \sim 1/T_2 \approx 1\,\text{kHz}$, with the detuned protocol still achieving single-spin sensitivity at a mere 115 Hz hyperfine coupling, a performance enhancement by a factor of 60. Conversely, a statistically polarized ensemble of 100 ^{13}C spins would be detectable from a distance of approximately 26 nm, compared to approximately 6 nm for the resonant protocol (assuming that the spin coherence of Ref. [15] continues to hold).

VI. QUANTUM GATE SELECTIVITY

Finally, we consider the use of the DDrf gate sequence for qubit control [9,14,21]. The challenge is to realize a high-fidelity (two-qubit) gate on a selected nuclear spin, while avoiding crosstalk to other spins. First, we consider the selectivity of the gates starting from the above results [Eqs. (1)–(5)]. In Sec. VII, we simulate a realistic spin register and identify the parameter regime(s) in which high-fidelity gates are possible.

We identify two selectivity mechanisms for the DDrf gate: selective driving due to the limited bandwidth of a single rf pulse [Fig. 5(a)] and the constructive build-up of small rotations due to the phase-increment condition being met for a specific nuclear spin [Fig. 5(b)]. Selective control can be achieved through either mechanism or through a combination thereof [see, e.g., Figs. 5(c) and 5(d)]. To quantitatively study these mechanisms, we consider a target nuclear-spin qubit t and a second, bystander, nuclear spin b for which crosstalk is to be avoided.

For the selectivity stemming from the individual rf pulses, Eq. (5) can be used directly to yield the smallest difference in nuclear-spin transitions for which $\tilde{\Omega}_b = 0$:

$$\left|\Delta^t_{0/1} - \Delta^b_{0/1}\right| \gtrsim \frac{\pi}{\tau}. \tag{10}$$

The superscripts t and b are used to denote the target and bystander spins, respectively, and the "0/1" subscript implies that this condition must hold for any combination of the ω_0 and ω_1 transitions. Evidently, the selectivity stemming from the rf pulses is limited by their bandwidth (approximately $1/\tau$), and the proximity of the nuclear-spin transitions. For the NV electron-spin-1 system considered here, the minimum difference between nuclear-spin hyperfine couplings required for achieving selectivity within a single rf pulse is

$$\left|A^t_{\parallel} - A^b_{\parallel}\right| \gtrsim \frac{\pi}{\tau}. \tag{11}$$

Next, to describe the selectivity due to the phase increments, it is instructive to realize that the phase increments effectively modulate the bare rf frequency (also known

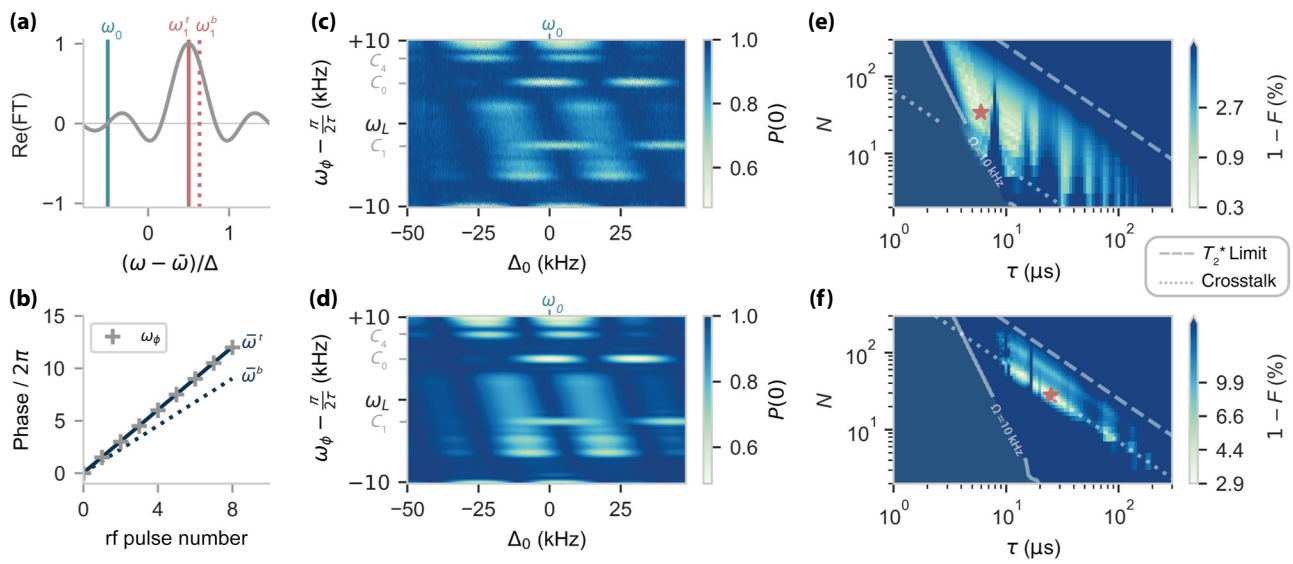

FIG. 5. Quantum gate selectivity. (a) A schematic as in Fig. 1(c). Due to their high bandwidth, single rf pulses may drive transitions of bystander spins (ω_1^b, dotted line), potentially inducing crosstalk [Eq. (10)]. (b) A schematic showing the phase build-up for the target spin (solid blue line) and the bystander spin (dotted blue line). The target spin can be selectively addressed by implementing the appropriate phase increment (gray crosses, Eq. (3), for clarity plotted without the extra π increments). (c) Experimental spectroscopy data as in Fig. 2(a), with different $\tau = 24.654\,\mu$s. Plotting the data as a function of the phase-increment frequency ω_ϕ [Eq. (12)] and Δ_0 highlights the different selectivity mechanisms. Nuclear spins appear at $\omega_\phi - \pi/(2\tau) = \bar{\omega}$ (linewidth approximately $(2N\tau)^{-1}$), modulated along the Δ_0 ($\propto \omega_{\rm rf}$) axis by their effective Rabi frequency (C_0, C_1, and C_4 resonances annotated). The bandwidth of the y axis (here, approximately 20 kHz) is set by the π/τ periodicity of Δ_ϕ, resulting in aliases that can cause spins to overlap. The jagged artifacts are due to the limited resolution of the data (taken as a function of δ_ϕ). (d) Simulation of (c) (see Appendix C). (e) A numerical simulation of the maximum attainable DDrf gate fidelity for nuclear spin C_1 in a six-spin register (including C_0, C_1, C_4, C_6, and C_8; see Table I). The fidelity is calculated for the full six-qubit unitary (the red star denotes the optimal parameters). The dotted line indicates $2N\tau = 131\,\mu$s, the minimum gate time that satisfies the selectivity bound [Eq. (15)]. The dashed line indicates $2N\tau = 5$ ms, corresponding to the limit on the gate time imposed by the nuclear-spin T_2^*. The color bar has logarithmic spacing. (f) A simulation for C_4, a more weakly coupled and spectrally crowded spin, resulting in lower fidelities. Here, the dotted line indicates $2N\tau = 1.4$ ms.

as "phase ramping" [36]), so that we can define a phase-increment frequency:

$$\omega_\phi = \omega_{\rm rf} + \frac{\delta_\phi}{2\tau}. \tag{12}$$

We can then rewrite the phase-increment resonance condition [Eq. (3)] as

$$\omega_\phi = \bar{\omega} + \frac{(2k+1)\pi}{2\tau}, \tag{13}$$

with $k \in \mathbb{N}$. Here, selectivity arises due to the difference in the mean frequencies $\bar{\omega}$ of the target and bystander spins, which has to be large enough for selective control.

A lower bound on the mean frequency difference can be attained by considering the Fourier-limited frequency resolution of the phase ramp (determined by its length of approximately $1/(2N\tau)$):

$$\left|\left(\bar{\omega}^t \mod \frac{\pi}{\tau}\right) - \left(\bar{\omega}^b \mod \frac{\pi}{\tau}\right)\right| \gtrsim \frac{\pi}{N\tau}, \tag{14}$$

where ω^t and ω^b denote the mean frequency of the target and bystander spins, respectively, and the modulo stems from the π/τ periodicity in Eq. (13). Although, strictly speaking, Eq. (14) constitutes an upper bound to the selectivity, it allows for a potential selectivity enhancement by a factor of N compared to Eq. (10). Whether such an enhancement is possible in practice depends on the spectrum of $\bar{\omega}$ for the electron-nuclear-spin system of interest. For example, for a spin-1/2 defect spin, the left-hand side of Eq. (14) vanishes, up to second-order corrections due to the perpendicular hyperfine component $A_\perp$ [29–31].

For the spin-1 system considered here, an exact bound for the selectivity can be derived, under the assumption of negligible driving in the electron $|0\rangle$ state (see Appendix H). In particular, fixing $\Omega N\tau = \pi/2$ to create a fully entangling gate, the condition for a selective gate on the target spin is given by

$$\left|\left(\frac{A_\parallel^t}{2} \mod \frac{\pi}{\tau}\right) - \left(\frac{A_\parallel^b}{2} \mod \frac{\pi}{\tau}\right)\right| \gtrsim \frac{\sqrt{15}\pi}{4N\tau}. \tag{15}$$

To illustrate the selectivity mechanisms, we again perform DDrf spectroscopy [similar to Fig. 2(a)] but instead of δ_ϕ, we now plot the data as a function of $\omega_\phi - \pi/(2\tau)$ [Figs. 5(c) and 5(d)]. This is a useful quantity, as it is independent of the rf frequency and directly relates to the mean frequency of a spin. Spins appear at their $\bar{\omega}$ frequency along the ω_ϕ axis (mod π/τ), with their signal intensity modulated by the effective Rabi frequency [Eq. (5)], which varies with Δ_0 (x axis). The signal from the spin bath (slanted bandlike features) is pushed away from $\Delta_0 = 0$ due to the form of Eq. (5) in the weak-coupling regime (Sec. IV).

The widths of the spin response along both axes partly determine if the spin can be selectively controlled or overlaps with other spins (crosstalk), as given in Eqs. (11) and (15). The π/τ periodicity of ω_ϕ creates opportunities for unexpected crosstalk to occur. For example, both the ω_0 and ω_1 transition of nuclear spin C_1 ($\Delta = -45.9$ kHz; Table I) somewhat overlap with sidelobes of the spin bath, limiting the expected gate fidelity of that spin for these gate parameters. In contrast, the transitions of spin C_0 ($\Delta = -30.7$ kHz; Table I) are not affected by such crosstalk, due to the particular value of τ used here. Note that for electron spin-1/2 systems, all nuclear spins will appear at approximately $\omega_\phi - \pi/(2\tau) = \omega_L$ (up to second-order corrections due to $A_\perp$), so that selective control depends more on whether spins can be resolved along the Δ_0 axis [29].

VII. A MULTIQUBIT NUCLEAR-SPIN REGISTER

We apply the insights from Sec. VI to investigate the boundaries of the gate parameter space that allows for high-fidelity control in a multiqubit nuclear-spin system. Considering the 15 identified spins near this NV center (Table I), we select a register of five nuclear spins that are most isolated in frequency space (Appendix I).

For a register with M nuclear spins, the ideal operation is given by

$$U_i = \mathrm{CR}_x(\pm\pi/2) \otimes \mathbb{I}^{\otimes(M-1)}, \tag{16}$$

where the controlled rotation acts on the electron and target spin subspace.

In addition to the unitary evolution of the six-qubit register dictated by $H_{\rm rf}$ [Eq. (2)], we include three additional contributions to the infidelity (see Appendix I): (i) the electron-spin T_2 dephasing time under DD (phenomenological; taken from Abobeih *et al.* [15]); (ii) electron-spin dephasing due to the direct interaction [Eq. (2)] with the characterized nuclear spins outside the register and the nuclear spin bath (in a mixed state); and (iii) $T_2^\star$ dephasing (approximately 10 ms [14]) of the nuclear spins in the register, simulated as quasistatic magnetic field noise. As is commonly done in experimental settings, we introduce a postgate echo pulse on the register spins to partially mitigate this dephasing [14,21]. Additionally, we restrict the rf amplitude to a maximum value of $\Omega = 10$ kHz (as in Sec. V).

To identify the optimal gate parameters, we vary the interpulse delay τ and the number of pulses N, while ensuring that the rf amplitude Ω is set to create the desired $\pm\pi/2$ rotation (compensating for the reduction in effective Rabi frequency using Eq. (5)). We set $\omega_{\rm rf}$ to the ω_1 transition of the target spin and calculate δ_ϕ accordingly [Eq. (3)], applying a second-order correction due to the ac Stark shift (Appendix D).

We obtain (six-qubit) average gate fidelity maps [37], such as those presented in Figs. 5(e) and 5(f), for target nuclear spins C_1 and C_4, respectively (Table I). We identify the following bounds on the available parameter space for high-quality gates. First, the maximum gate time is limited by nuclear- and electron-spin decoherence, the latter of which depends on N and τ. A minimum gate time is dictated by the degree of spectral crowding of the target spin, as predicted by Eq. (14). Contrary to C_1, C_4 is spectrally close to another spin (C_3, approximately 1.4 kHz), so that high-fidelity gates are only found for larger gate times ($2N\tau \gtrsim 1.4$ ms). In particular, through the definition of the selectivity (see Appendix H), equalizing Eq. (15) [dotted line in Fig. 5(f)] ensures zero crosstalk with the nearest bystander spin (C_3).

Furthermore, even though the reduction in effective Rabi frequency $\tilde{\Omega}$ can in principle be fully compensated for, when $\Omega \sim \Delta$, the assumptions underlying Eq. (5) break down (Appendix K) and our prediction for the optimal gate parameters no longer produces high-fidelity gates [top-left corner of Figs. 5(e) and 5(f)]. For spins with smaller hyperfine couplings (e.g., C_4), this effect is more detrimental to the maximum attainable fidelity. Finally, the remaining parameter space is interspersed with sharp drops in fidelity at τ values for which crosstalk occurs with other individual spins or with the nuclear spin bath. The combination of these effects results in maximum six-qubit gate fidelities of $F = 99.7\%$ and $F = 97.1\%$ for target spins C_1 and C_4, respectively. For the other register spins and breakdowns of the different infidelity contributions, see Appendix I.

Note that here we have not optimized ω_{rf}, which could further reduce crosstalk and realize improved effective Rabi frequencies (see Sec. V).

VIII. CONCLUSIONS

In conclusion, we have presented an improved and generalized framework for electron-nuclear DDrf gates. Our model reveals that these gates can be deconstructed into two independent components: (1) the driving induced by individual rf pulses [Eq. (5)] and (2) the rf phase increments that enable constructive rotational build-up throughout the sequence [Eq. (3)]. Considering these components independently allows for increased versatility in gate optimization for sensing and quantum control (e.g., by detuning the rf frequency) but also reveals inherent limitations in the gate speed and selectivity.

A first, general, insight is that the *effective* Rabi frequency for short interpulse delays ($\Delta\tau \lesssim \pi$) can be strongly suppressed for conditional gates and enhanced for unconditional gates. This reveals an inherent trade-off between protecting electron-spin coherence by faster decoupling and retaining nuclear-spin selectivity and gate efficiency. This trade-off has important implications for the sensing and control of nuclear spins, including in typical physical systems, such as for an electron spin in a dilute nuclear spin bath [5,7,21,23,30]. The detuned sensing scheme presented partially compensates for this reduction in Rabi frequency, making DDrf a promising alternative to conventional DD spectroscopy in the context of nano-NMR [12,18,38]. Future work might extend this principle to high-fidelity quantum gates.

A second key insight is that quantum gate selectivity stems both from direct rf driving of the spin transition frequencies, as well as the targeting of the mean spin evolution frequency by the phase increments. Importantly, for systems in which the mean nuclear-spin frequencies are first-order degenerate (e.g., electronic spin-1/2 systems), the rf pulses can still provide a selectivity mechanism, albeit limited by their bandwidth (see also Beukers *et al.* [29]). A possible improvement may consist of creating intermediate evolution periods with a nuclear-spin frequency that is dependent on the electron-spin state; e.g., by temporarily swapping the electron-spin state to a memory qubit [29].

These results provide new opportunities for the optimization of quantum gate fidelities for quantum information processing and quantum network applications [2,9,21, 39–41]. They are applicable to a large variety of systems, such as various spin defects in diamond [29,30], silicon [25] and silicon carbide [23,42], and might also be transferable to other platforms such as quantum dots [43] and rare-earth ions [44].

ACKNOWLEDGMENTS

We thank H. P. Bartling and C. E. Bradley for useful discussions. We gratefully acknowledge support from the joint research program "Modular quantum computers" by Fujitsu Limited and Delft University of Technology, co-funded by the Netherlands Enterprise Agency under Project No. PPS2007. We acknowledge financial support from the Quantum Internet Alliance through the Horizon Europe program (Grant Agreement No. 101080128). This project has received funding from the European Research Council (ERC) under the European Union (EU) Horizon 2020 research and innovation program (Grant Agreement No. 852410). This work was supported by the Dutch National Growth Fund (NGF), as part of the Quantum Delta NL program. This work is part of the research program Research along Routes by Consortia (NWA-ORC) with Project No. NWA.1160.18.208, which is (partly) financed by the Dutch Research Council (NWO). This project has received funding from the EU Horizon Europe research and innovation program under Grant Agreement No. 101135699.

H.K.C.B., C. Waas, R.H., T.H.T., H.B.v.O., and N.D. have filed a patent for a method of increasing the selectivity of a nuclear-spin gate, by interleaving the gate by

periods in which the electron resides in an eigenstate, while its state is stored in a quantum memory.

DATA AND CODE AVAILABILITY

All data underlying the study are available on the open 4TU data server [45]. The code used for performing the numerical simulations and for operating the experiments is available on request.

APPENDIX A: EXPERIMENTAL METHODS

All experiments are conducted on a naturally occurring NV center using a custom-built cryogenic confocal microscopy setup (4K, Montana Cryostation). The diamond sample, which has a natural abundance of 1.1% ^{13}C, has been homoepitaxially grown via chemical vapor deposition (Element Six) and cleaved along the $\langle 111\rangle$ crystal direction.

A solid immersion lens (SIL) is milled around the NV center to improve photon-collection efficiency [46]. A gold stripline is deposited near the edge of the SIL for the application of microwave (MW) and rf pulses. Typical nuclear Rabi frequencies can reach up to approximately 1.6 kHz, above which sample heating starts to affect the NV readout. MW and rf signals are generated by a ZI HDAWG Arbitrary Waveform Generator, in combination with a MW mixer and separate rf and MW amplifiers. An external magnetic field of $B_z = 189.1$ mT is applied along the NV-symmetry axis, using a permanent neodymium magnet mounted to the back of the cryostat cold finger. An external permanent magnet is used for fine alignment of the magnetic field: the small remaining perpendicular magnetic field components are neglected here.

The NV spin state is initialized via spin pumping and read out in a single shot through spin-selective resonant excitation, with fidelities $F_0 = 0.930(3)$ ($F_1 = 0.995(1)$) for the $m_s = 0$ ($m_s = -1$) state, respectively, resulting in an average fidelity of $F_{\text{avg}} = 0.963(3)$. The reported data are corrected for these numbers to obtain a best estimate of the electronic spin state. We drive the electronic $m_s = 0 \leftrightarrow m_s = -1$ spin transition at 2.425 GHz with Hermite-shaped pulses.

In this work, sequences of XY-8 type are used for DD during the DDrf gate, to minimize the effects of pulse errors [15]. The lengths of the rf pulses in the DDrf sequences in this work are set to an integer number of periods of the rf radiation, to prevent the NV electron spin from picking up extra phase. Each rf pulse has a $\sin^2(t)$ roll-on and roll-off to prevent signal ringing in the rf signal chain, with a roll duration of two rf periods. Due to this pulse shaping, the two rf pulses of length τ in the DDrf sequence create a smaller combined rotation than the rf pulses of length 2τ. To correct for this, the amplitude of the single-τ pulses is multiplied by the ratio of the integrals of the 2τ pulse and the two single-τ pulses.

DDrf spectroscopy [Figs. 2, 3 and 5(c)] is performed by (i) preparing the electron spin in the $m_s = 0$ state; (ii) applying a $\pi/2$ MW pulse on the electron spin to prepare the $|+\rangle$ state; (iii) performing the DDrf sequence; (iv) applying a $-\pi/2$ MW pulse (the same axis as the initial $-\pi/2$ pulse); and (v) reading out the electron spin state. The experiment is repeated to estimate $P(0)$, the probability of finding the electron in the $m_s = 0$ state. $P(0)$ corresponds to the remaining electron-spin coherence after the DDrf sequence.

APPENDIX B: NV HAMILTONIAN

The NV center is described by a spin-1 electron coupled to a spin-1 nitrogen spin, with additional couplings to spin-1/2 ^{13}C spins. The interaction with the spin-1 nitrogen spin is neglected, as it is initialized in the $m_N = 0$ state and the decoupling sequences effectively cancel the interaction between the electron and nitrogen spins. Considering one ^{13}C spin, the Hamiltonian of the system is, in the interaction picture and after the rotating-wave and secular approximation, given by

$$H = \omega_0 I_z + A_\parallel S_z^1 I_z + A_\perp S_z^1 I_x + 2\Omega\cos(\omega_{\text{rf}} t + \phi) I_x, \tag{B1}$$

where $A_\parallel = A_{zz}$ and $A_\perp = \sqrt{A_{zx}^2 + A_{zy}^2}$ are the parallel and perpendicular components of the NV-nuclear hyperfine tensor, S_z^1 is the electron spin-1 operator, I_z and I_x are the nuclear-spin-1/2 operators, Ω is the physical rf amplitude, ω_{rf} is the rf frequency, and ϕ is some phase offset of the rf field. In this work, only the $m_s = \{0, -1\}$ subspace of the electron spin is considered.

Note that, in general, the axis of $A_\perp$ and the axis along which the rf radiation is applied are not the same. In the present work, for simplicity, the effect of $A_\perp$ is neglected. This is motivated by the high magnetic field (189.1 mT) at which the experiments are performed, due to which the nuclear Larmor frequency is much larger than the NV-nuclear hyperfine interaction strength of spins considered in this work. In this case, the tilt of the nuclear quantization axis is small ($<1^\circ$ for $A_\perp \sim 30$ kHz). For simulations of the impact of $A_\perp > 0$ on gate fidelities, see Bradley *et al.* [14] and Hannes *et al.* [28]. We do take into account the changed nuclear precession frequency due to $A_\perp$, given by: $\omega_1 = \sqrt{A_\perp^2 + (\omega_0 - A_\parallel)^2}$.

In the rotating frame at the rf frequency (and again making the rotating-wave approximation), Eq. (B1) simplifies to

$$H_{\text{rf}} = |0\rangle\langle 0| \otimes \Delta_0 I_z + |1\rangle\langle 1| \otimes \Delta_1 I_z + \mathbb{I} \otimes \Omega(\cos\phi I_x + \sin\phi I_y), \tag{B2}$$

APPENDIX C: SIMULATION OF DDrf SPECTROSCOPY

Spectroscopy experiments [Figs. 2(b) and 5(d)] have been simulated assuming the presence of 15 individual nuclear spins (Table I) and a bath of weakly coupled spins.

For an individual nuclear spin c, the unitary operation U of an $N = 2$ DDrf unit cell has been calculated starting from $H_{\rm rf}$ [Eq. (2)]. For starting electron state $|0\rangle$ ($|1\rangle$), the rotation axis $\hat{\mathbf{n}}_{0,c}$ ($\hat{\mathbf{n}}_{1,c}$) and angle $\theta_{0,c}(=\theta_{1,c})$ of the nuclear-spin rotation have been determined. If the electron spin starts in the $|x\rangle$ state, the $\langle\sigma_x\rangle_c$ expectation value after a DDrf gate with N pulses is given by [12]

$$\langle\sigma_x\rangle_c = 1 - (1 - \hat{\mathbf{n}}_{0,c}\cdot\hat{\mathbf{n}}_{1,c})\sin^2\frac{N\theta_c}{2}. \tag{C1}$$

The total signal from the individual spins is given by the product of the expectation values:

$$\langle\sigma_x\rangle = \prod_c \langle\sigma_x\rangle_c\,. \tag{C2}$$

For the nuclear spin bath, a mean density of parallel hyperfine shifts Δ is used [7]:

$$\rho(\Delta) = \frac{\pi^2\alpha\rho_{^{13}\mathrm{C}}}{\Delta^2}, \tag{C3}$$

where $\alpha = \hbar\mu_0\gamma_e\gamma_c/4\pi$ and $\rho_{^{13}\mathrm{C}} = n_{13}\rho_{\mathrm{C}} = 1.950\,\mathrm{nm}^{-3}$ is the density of ^{13}C in natural-abundance diamond, where n_{13} is the relative abundance of ^{13}C atoms in the environment (1.109%) and ρ_{C} is the density of C atoms in diamond.

Instead of calculating the bath signal for a random sample of individual spins [15], we calculate the signal for a sufficient number of bins (300 in this work) of Δ of width $d\Delta$. The expected number of spins in such a bin is given by $\rho(\Delta)\,d\Delta$. The spectroscopy signals for each bin $\langle\sigma_x(\Delta)\rangle$ are calculated using Eq. (C1) and combined to yield the total signal of the spin bath:

$$\langle\sigma_x\rangle_{\mathrm{bath}} = \prod_{\Delta=-\Delta_{\mathrm{lim}}}^{\Delta_{\mathrm{lim}}} \langle\sigma_x(\Delta)\rangle^{\rho(\Delta)\,d\Delta}, \tag{C4}$$

TABLE I. The characterized nuclear-spin hyperfine shifts. Spins marked with a superscript ([a]) form the register considered in Sec. VI.

Index	Δ (Hz)	Index	Δ (Hz)	Index	Δ (Hz)
C_0^{a}	−30 693	C_5	−12 570	C_{10}	−9500
C_1^{a}	−45 870	C_6^{a}	15 744	C_{11}	−9000
C_2	20 000	C_7	-10 020	C_{12}	-13 060
C_3	19 900	C_8^{a}	−11 160	C_{13}	−6193
C_4^{a}	18 500	C_9	−7660	C_{14}	−7200

where Δ_{lim} defines the maximum coupling strength of spins that are still considered part of the spin bath, in this work $\Delta_{\mathrm{lim}} = 2\pi \times 6\,\mathrm{kHz}$. Note that this approach breaks down when the signal due to a single spin with Δ becomes large. The total signal is given by the product of the signals of individual spins and the spin bath.

The Rabi frequency Ω has been determined from the waveform amplitude of the rf pulses and an experimentally determined conversion factor from the waveform amplitude to Ω. The pulse length τ_{rf} is adjusted by half the length of the pulse roll-on time (Appendix A) to approximately account for the smaller effective pulse amplitude and the dead time around the MW pulses is subtracted. The rf Hamiltonian is applied for a duration of τ_{rf} and during the dead time we set $\Omega = 0$. The simulation could be made more accurate by considering a time-dependent Ω, matching the pulse shape, at the cost of computation time.

From the spectroscopy signal, we qualitatively identify 15 individual nuclear spins that can be distinguished from the spin bath (listed in Table I).

APPENDIX D: THEORETICAL FIDELITY OF DETUNED GATES

We present a closer study of the theoretically achievable fidelity of DDrf gates on a single nuclear spin, neglecting $A_\perp$. We consider the spin and gate parameters from Fig. 2(c): $\Delta = -30.7\,\mathrm{kHz}$, $\tau = 24.654\,\mu\mathrm{s}$, and $\Omega = 313\,\mathrm{Hz}$. We numerically calculate the DDrf gate unitary U using H_{rf} [Eq. (2)] and compare it to the ideal unitary

$$U_{\mathrm{ideal}} = |0\rangle\langle 0| \otimes R_x(\pi/2) + |1\rangle\langle 1| \otimes R_x(-\pi/2). \tag{D1}$$

To compare U and U_{ideal}, we decompose U into its rotation angle θ and rotation axes $\hat{\mathbf{n}}_0$ and $\hat{\mathbf{n}}_1$, for each starting electron spin state (see more detail in Appendix J). We then calculate

$$U' = |0\rangle\langle 0| \otimes e^{-i(\pi/2)\hat{\mathbf{n}}_0\cdot\vec{\sigma}} + |1\rangle\langle 1| \otimes e^{-i(\pi/2)\hat{\mathbf{n}}_1\cdot\vec{\sigma}} \tag{D2}$$

and compare that to U_{ideal} (Fig. 6). This assumes that the rotation angle of the gate can be tuned to be $\pi/2$, which could be achieved experimentally with a calibration sequence. Tuning the rotation angle with N has no effect on $\hat{\mathbf{n}}_{0,1}$ and fine tuning with Ω would only slightly affect $\hat{\mathbf{n}}_{0,1}$.

First, we consider resonant and off-resonant DDrf gates [Fig. 6(a)]. We find that high gate fidelities ($F > 0.999$) are achievable for a wide range of detunings. To maximize the gate fidelity, it is necessary to adjust the single-pulse phase increment δ_ϕ slightly from the previously derived resonance condition [Eq. (3)].

Increasing the Rabi frequency reveals why the optimal δ_ϕ changes [Fig. 6(b)]. When driving on resonance ($\Delta_1 =$

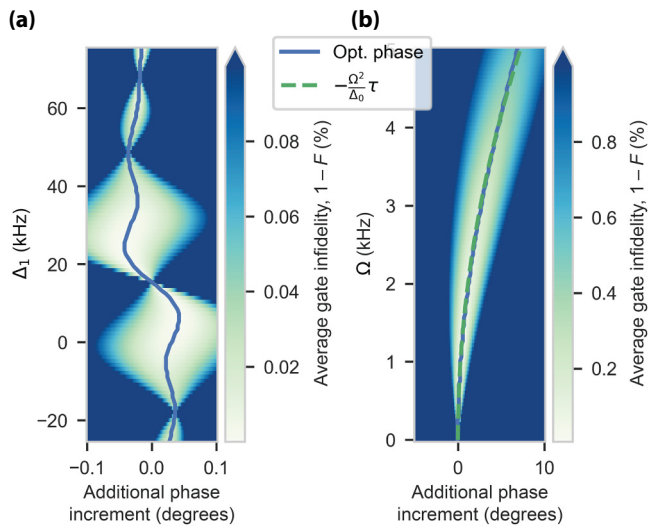

FIG. 6. The optimal single-pulse phase increment. (a) The average gate infidelity of a DDrf gate, over a range of rf detunings Δ_1 and phase increments δ_ϕ. The phase increment on the x axis is added to the resonant δ_ϕ as derived in Eq. (3). The optimal phase increment (that yielding the highest fidelity) varies with the applied rf frequency. (b) As a function of the Rabi frequency Ω, the optimal phase increment for a gate on resonance with one of the nuclear-spin frequencies (here, $\Delta_1 = 0$) can be predicted using the ac Stark shift.

0), the optimal phase increment is shifted by

$$\delta_{\rm ac} = -\frac{\Omega^2}{\Delta_0}\tau. \tag{D3}$$

We attribute this effect to the ac Stark shift [36]. The presence of rf radiation at the ω_1 frequency causes the ω_0 frequency of the nuclear spin to shift, resulting in a different amount of phase being picked up by the spin while the electron is in the $|0\rangle$ state. For other rf frequencies, a combined effect of shifting both nuclear-spin resonance frequencies occurs.

APPENDIX E: EXPRESSION FOR THE SENSITIVITY

We define the single-spin sensitivity according to Ref. [33]:

$$\upsilon_{\rm min} = \frac{e^{\chi(t)}\sqrt{t+t_m}}{\gamma C(t_m)t}, \tag{E1}$$

where t is the single-experiment sensing time, t_m is the readout time, C is a readout-efficiency parameter, γ is the signal-transduction parameter, and $\chi(t)$ is the coherence function of the sensor spin. For simplicity, we assume an ideal instantaneous readout ($C = 1, t_m = 0$). For the system under study here, this assumption is reasonable as the (single-shot) readout fidelity is $\gtrapprox 90\%$ and the readout time ($t_m < 50\,\mu$s) is significantly shorter than the typical sensing time ($t \sim 1$ ms) [14]. In our case, γ is equal to the (effective) Rabi frequency $\tilde{\Omega}/(2\pi)$ and has units of Hz/spin, as a single nuclear spin induces phase on the sensor at this rate. Equation (E1) then reduces to

$$\upsilon_{\rm min} = \frac{2\pi e^{\chi(N,t)}}{\tilde{\Omega}_{\rm max}(\Delta, N)\sqrt{t}}, \tag{E2}$$

which is equivalent to Eq. (8).

Note that the electron coherence function $\chi(N,t)$ during the DDrf sequence is dependent on the number of applied decoupling pulses N [15],

$$\chi(N,t) = \left(\frac{t}{T(N)}\right)^n, \tag{E3}$$

with $n = 2$, and the coherence time $T(N)$, given by

$$T(N) = T_{N=4}\left(\frac{N}{4}\right)^\eta, \tag{E4}$$

with $T_{N=4} = 2.99$ ms and $\eta = 0.799$ [15].

APPENDIX F: OPTIMAL rf DETUNING

The optimal rf detuning condition for a specific Δ and τ is found by choosing Δ_1 (and the corresponding $\Delta_0 = \Delta_1 - \Delta$), so that Eq. (5) is maximized. As Eq. (5) and its derivatives are transcendental, it is not trivial to find these maxima. Therefore, we look for an approximate solution, by considering the behavior of the function in the limit of long and short τ.

In the limit of long τ (defined as $\tau \gg 2\pi/|\Delta|$), the optimal detuning is (trivially) $\Delta_1 = 0$. In this limit, the two sinc functions in Eq. (5) are completely separated and the global maximum is simply the maximum of the sinc function centered around ω_1 [Fig. 7(a)].

However, for short τ, the spectral width of the sinc functions increases, so that they interfere destructively, which pushes the optimal detuning condition outward [Fig. 7(a)]. In the short-τ limit ($\tau \ll 2\pi/|\Delta|$), we can conceptually see that maximum $\tilde{\Omega}$ will be attained when the difference in driving between the ω_0 and ω_1 transitions is largest, as this maximizes the conditional character of the gate. For the square rf pulses considered in this work, this condition is satisfied when the sinc pulse envelope has maximum gradient at $\bar{\omega} = (\omega_1 + \omega_0)/2$ [schematically illustrated in Fig. 4(a)]. By evaluating the second derivative of the sinc function, we find that the (maximum-gradient) inflection point is located at a distance w_s away from the peak center, with $w_s \approx 2.082$ the first root of the second derivative of the sinc function. Requiring this point to be positioned precisely in between the two transitions (i.e. $\Delta/2$ away

from ω_1), we arrive at the condition

$$\Delta_1 = -\frac{w_s}{\tau} + \Delta/2. \tag{F1}$$

It is not *a priori* obvious that these two limiting cases perform well in describing the optimal condition in the intermediate regime ($\tau \sim 2\pi/|\Delta|$). To evaluate the validity of the limiting cases and to investigate their performance in the intermediate regime, we compute Eq. (5) for a range of τ values [Fig. 7(a)] and numerically extract its maximum value [Fig. 7(b), solid blue line]. We compare this numerical value to a composite function, generated by joining the limiting descriptions at condition $\tau = 2\pi/|\Delta|$:

$$\Delta_1 = \begin{cases} -\frac{w_s}{\tau} + \Delta/2, & \text{if } \tau \lesssim 2\pi/|\Delta|, \\ 0, & \text{otherwise,} \end{cases} \tag{F2}$$

which is equivalent to Eq. (9). We find good agreement between the numerical maximum and the effective Rabi frequency obtained by inserting Eq. (F2) into Eq. (5), which yields

$$\tilde{\Omega}/\Omega = \begin{cases} \mathrm{sinc}\left(w_s - \frac{\Delta\tau}{2}\right) - \mathrm{sinc}\left(w_s + \frac{\Delta\tau}{2}\right), & \text{if } \tau \lesssim 2\pi/|\Delta|, \\ 1 - \mathrm{sinc}(\Delta\tau), & \text{otherwise.} \end{cases} \tag{F3}$$

We observe only a $< 5\%$ deviation between Eq. (F3) and the maximum of Eq. (5) across the full range [Fig. 7(b), dotted blue line]. Thus, we conclude that Eq. (F2) is suitable for finding the optimal rf detuning in a sensing setting.

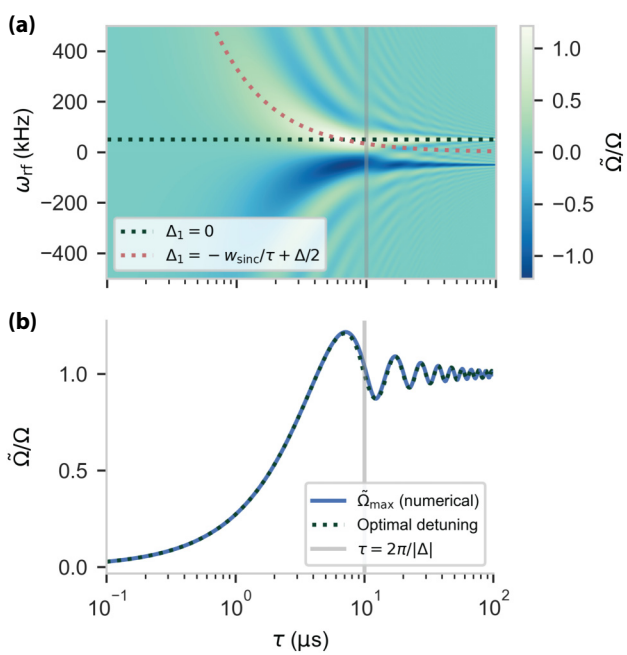

FIG. 7. Optimal rf detuning. (a) Equation (5) is evaluated for a range of interpulse spacings τ, sweeping the rf detuning (by varying ω_{rf}). The simulated nuclear spin has a hyperfine coupling $\Delta = 50$ kHz. The dotted dark green line indicates resonant driving, while the dotted red line indicates the (optimal) rf detuning in the regime $\tau < 1/\Delta$ (solid gray line). (b) The maximum (relative) effective Rabi frequency as a function of τ, computed by taking the maximum value in (a) (solid blue line). We find good agreement with the analytical (maximum) expression, obtained by evaluating Eq. (5) with rf detuning described by Eq. (9) (dotted blue line).

APPENDIX G: SENSING OPTIMIZATION PROCEDURE

To find the optimal sensing parameters, we follow the steps described in Fig. 7 and in the main text. First, we compute the effective Rabi frequency for a range of realistic N and τ values [15]. Then, we compute the optimal physical rf amplitude Ω. Ideally, this power is increased to exactly counter the reduction in the Rabi frequency. However, this requires setting the Rabi amplitude to very large values for small τ. As Eq. (5) is only valid in the regime $\Omega\tau \ll 1$, we limit the amplitude to $\Omega = \min[1/(2\tau), 10\,\text{kHz}]$. In Fig. 8(b), we show the set rf amplitude under this limitation. In the bottom-right region of the graph, the modification of the Rabi frequency is small [see Fig. 8(a)] and therefore Ω is not increased significantly. In the top-left corner, however, the desired rf amplitude exceeds our set limits and its value is capped at 10 kHz. Note that the optimal sensing parameters depend on the precise choice of the limits. Therefore, it will be important to reevaluate these in practice, depending on the specific limitations of the experimental setup (e.g., rf delivery efficiency or cryogenics).

Next, the effective Rabi frequency is computed by multiplying the values obtained in Figs. 8(a) and 8(b). Then, we compute the expected electron coherence for all values of N and τ, based on the decoherence function from Ref. [15]. We compute the sensitivity according to Eq. (8) and plot its value, and its inverse, in Figs. 8(f) and 8(e), respectively. A sensitivity below one [blue region in Fig. 8(f)] means that the sequence is sensitive to a single nuclear spin.

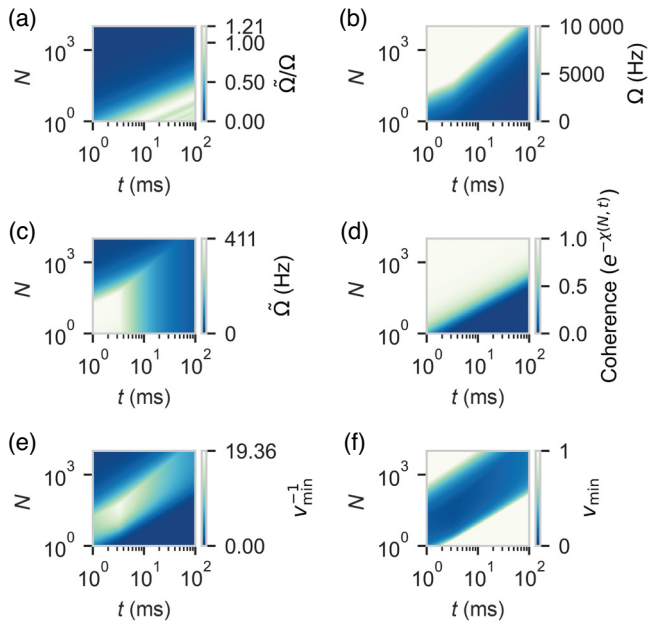

FIG. 8. Optimal parameters for sensing. (a) The relative effective Rabi frequency as a function of the total DDrf sequence length (t) and the number of applied electron pulses (N), obtained by evaluating Eq. (F3). (b) The physical rf amplitude Ω, which is set to counter the suppression of the Rabi frequency visible in (a). (c) The effective Rabi frequency, calculated by taking the product of (a) and (b). (d) The electron coherence function, taken from Ref. [15]. Adding more pulses (shortening the interpulse spacing τ) leads to increased electron coherence at constant gate time t. (e) The inverse of the sensitivity, defined in Eq. (8), calculated by multiplying (c) and (d). (f) The sensitivity function, showing a significant region where single-spin selectivity ($v_{\min} < 1$) is attainable. To generate the data in Fig. 4(d), we generate this plot for a range of Δ values and numerically pick the minimum value.

Finally, we generate these plots for a number of coupling strengths Δ, ranging from 30 Hz to 10 kHz, and numerically select the maximum value for the sensitivity. Then, we repeat the process without allowing for detuned driving, which results in significantly lower sensitivity. The results are shown in Fig. 4.

APPENDIX H: BOUND FOR GATE SELECTIVITY

We present a brief mathematical justification for the DDrf gate selectivity that accumulates over the duration of the gate [Eq. (14)]. If we assume negligible driving of the nuclear spin when the electron is in the $|0\rangle$ state (i.e., assuming that $\Delta_0\tau \gg \pi$, which also implies that $\Delta_0 \gg \Omega$, given that $\Omega\tau \ll 1$), the dynamics can be approximated by the Hamiltonian

$$H_{\mathrm{rf},|1\rangle} = |0\rangle\langle 0| \otimes \Delta_0 I_z + |1\rangle\langle 1| \otimes (\Delta_1 I_z + \Omega(\cos\phi I_x + \sin\phi I_y)). \tag{H1}$$

A compact expression for the spectroscopy response $\langle S_x\rangle$ of the electron spin can be found when the phase increment $\delta_\phi = -\Delta_0\tau + \pi$ (see Appendix J):

$$\langle S_x\rangle = \frac{1}{2}\left(1 - \frac{2}{1+\Delta_1^2/\Omega^2}\sin^2\left(\frac{N\tau}{2}\sqrt{\Omega^2+\Delta_1^2}\right)\right). \tag{H2}$$

Note that this δ_ϕ is the optimal phase increment when $\Delta_1 = 0$ [Eq. (3)]. For $\Delta_1 \neq 0$, and for $|0\rangle$ being the electron $m_s = 0$ state (giving all spins the same Δ_0), the above equation predicts the response of the electron spin to a bystander spin, which diminishes due to the mismatch between δ_ϕ and the actual evolution of the bystander spin. The minimum detuning Δ_1 between the bystander spin and the target spin that causes no crosstalk is given by the first zero of the response of the electron spin. Considering the case of an entangling gate between the electron and target spin ($\Omega N\tau = \pi/2$), there is no crosstalk if

$$\Delta_1 = \frac{\sqrt{15}\pi}{2N\tau}. \tag{H3}$$

Translating this to a difference in mean frequency results in

$$\frac{\Delta_0^t + \Delta_1^t}{2} - \frac{\Delta_0^b + \Delta_1^b}{2} = \bar{\omega}^t - \bar{\omega}^b = \frac{\sqrt{15}\pi}{4N\tau}. \tag{H4}$$

Furthermore, the selectivity can be argued from the Lorentzian factor $2/(1+\Delta_1/\Omega^2)$ in Eq. (H2). Under the entangling gate condition $\Omega = \pi/2N\tau$, this Lorentzian has a full width at half maximum of $\pi/N\tau$.

APPENDIX I: MULTIQUBIT-REGISTER OPTIMIZATION

In this appendix, we provide more details on the spin-register simulations (Fig. 5). The M two-qubit DDrf unitaries between the electron spin and each nuclear spin in the register are calculated using Eqs. (K1) and (K2). The unitaries are corrected for deterministic phase offsets on the idling qubits, which could be taken into account experimentally at no fidelity cost by calibrating virtual Z gates. The total $(M+1)$-qubit unitary U_c is subsequently constructed from these two-qubit unitaries, by extending them to the $(M+1)$-qubit register space and concatenating them, which assumes that they commute. The resulting unitary is an approximation that neglects nuclear-nuclear interactions, as well as electron-nuclear interactions with spins outside the register. Below, we will introduce the effects of such interactions in a phenomenological way. We also assume idealized (i.e., instantaneous) electron spin pulses that neglect the effect of the electron-nuclear coupling during the pulse.

The $(M+1)$-qubit gate fidelity is calculated according to

$$F(U_i, U_c) = \frac{\sum_j \mathrm{Tr}(U_i U_j^\dagger U_i^\dagger U_c U_j U_c^\dagger) + d^2}{d^2(d+1)}, \tag{I1}$$

where the summation j is over the Pauli matrices and d is the dimension of the Hilbert space [37].

To incorporate electron-spin dephasing, which commutes with the unitary U_c, a dephasing-error channel is applied after U_c. The single-qubit-error channel on the electron spin is given by the transformation

$$\epsilon(\rho) = \sum_i \hat{K}_i \rho \hat{K}_i^\dagger, \tag{I2}$$

with Kraus operators

$$\hat{K}_0 = \sqrt{\frac{(1+\lambda)}{2}}\,\hat{\mathbb{I}}, \quad \hat{K}_1 = \sqrt{\frac{(1-\lambda)}{2}}\,\hat{Z}. \tag{I3}$$

Leading to an error channel for the $(M+1)$-qubit unitary:

$$\epsilon_{M+1}(\rho) = \frac{(1+\lambda)}{2}\mathbb{I}^{\otimes(M+1)}\rho\,\mathbb{I}^{\otimes(M+1)} + \frac{(1-\lambda)}{2}(Z\otimes\mathbb{I}^{\otimes M})\rho(Z\otimes\mathbb{I}^{\otimes M}). \tag{I4}$$

The average gate fidelity of the operator U_c, followed by the dephasing channel ϵ_{M+1}, is then given by

$$F(U_i, U_c, \lambda) = \frac{(1+\lambda)}{2}F(U_i, U_c) + \frac{(1-\lambda)}{2}F(U_i, Z'U_c), \tag{I5}$$

where $Z' = Z \otimes \mathbb{I}^{\otimes M}$.

The parameter λ quantifies the dephasing of the electron spin, which may have one or more independent origins. Considering the dephasing due to the T_2 of the electron spin (λ_{T_2}, due to the nuclear-spin-bath dynamics) and the direct DDrf-gate-mediated interaction with (mixed) bath spins (λ_{bath}), the total dephasing is given by $\lambda = \lambda_{\mathrm{bath}}\lambda_{T_2}$, with

$$\lambda_{\mathrm{bath}} = \langle\sigma_x\rangle_{\mathrm{bath}}, \quad \lambda_{T_2(N,t)} = e^{-(t/T(N))^n}, \tag{I6}$$

where $\langle\sigma_x\rangle_{\mathrm{bath}}$ quantifies the rf-mediated electron dephasing due to the nuclear spin bath (see Appendix C) and $T_2(N,t)$ is the dephasing time of the electron spin during a DD sequence of N pulses and duration t (see Appendix E).

We implement $T_2^\star$ nuclear-spin dephasing, which does not commute with the unitary evolution during the DDrf gate, by sampling static magnetic field offsets δ_B from a Gaussian distribution with standard deviation $\sigma_B = 1/(\sqrt{2}\pi\gamma_c T_2^\star)$, where γ_c is the ^{13}C gyromagnetic ratio and $T_2^\star$ is the decoherence time for ^{13}C nuclear spins (approximately 10 ms). We calculate average gate fidelities

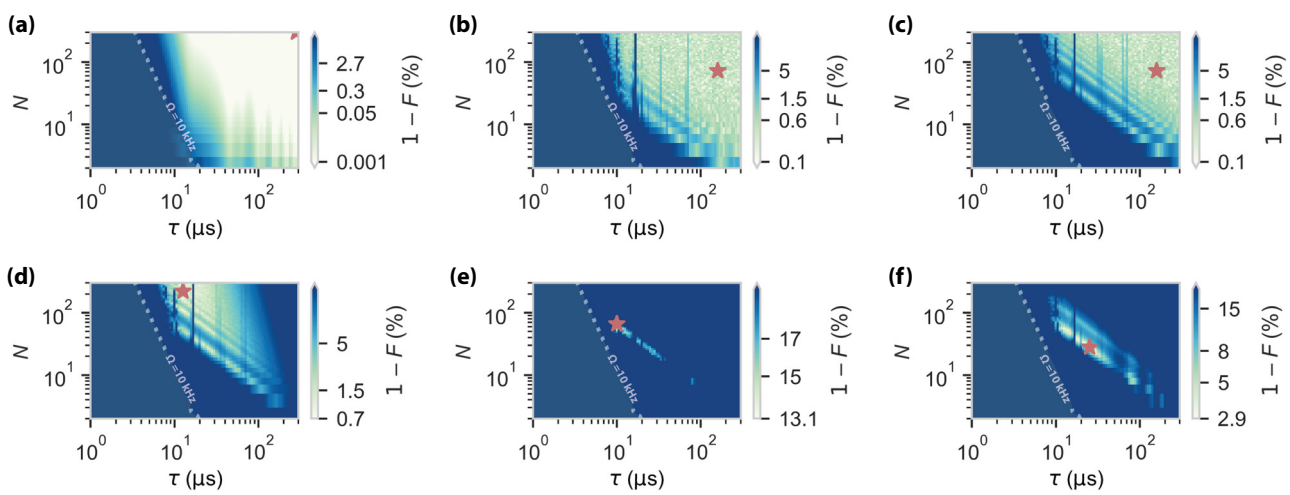

FIG. 9. The infidelity contributions to a two-qubit gate in a six-qubit register. F is the six-qubit gate fidelity. (a)–(e) The different contributions in infidelity with C_4 as target qubit. (a) Single spin: considering only the target, for which high-fidelity gates exist across the parameter space. The rf amplitude is limited to $\Omega < 10$ kHz (dotted line), resulting in a sharp fidelity drop-off. At larger N, the approximation used for obtaining Eq. (5) loses validity. (b) Register spins: considering the unitary evolution of all six spins in the register (from U_c). (c) Spin bath: also including the signal of a sampled spin bath, using Eq. (C4) for λ_{bath} [Eq. (I6)] and the remaining identified individual bystander spins (Table I) (d) T_2^e: also including the electron-spin T_2 dephasing under DD [Eq. (I6)], which limits both τ and the gate times. (e) $T_{2,c}^\star$: also including the $T_2^\star$ dephasing of the nuclear-spin-register qubits by averaging over a distribution of magnetic fields δ_B. This hinders the performance, both by stochastic detuning of the target qubit operation and by direct dephasing of the register. (f) Nuclear-spin echo: also including a correction on the phase of all register qubits [Eq. (I7)], akin to performing a spin-echo operation on all register qubits, meant to decouple the qubits from quasistatic noise [14,21].

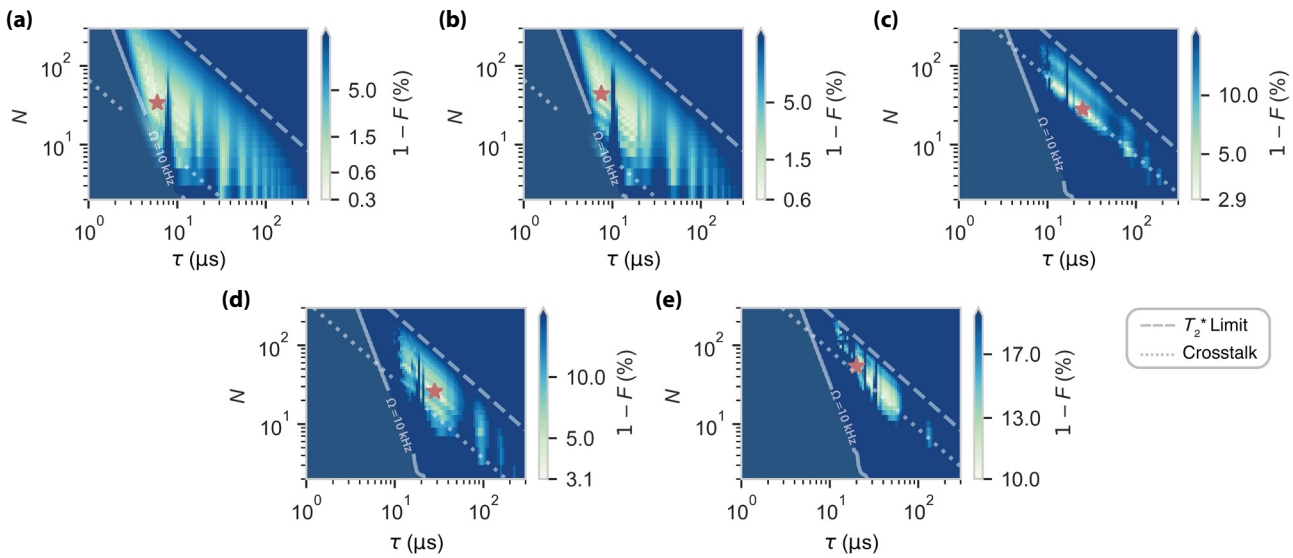

FIG. 10. The characterization for all five electron-nuclear-spin-controlled gates in the six-qubit register: (a) C_1; (b) C_0; (c) C_4; (d) C_6; (e) C_8. For each nuclear spin participating in the register, we calculate the six-qubit average gate fidelity for the U_i gate, given by Eq. (I5). The τ for which crosstalk occurs with other nuclear spins is different for each target spin. The spectral isolation of a spin sets a minimum gate length (dotted lines, Eq. (11)) and the nuclear spin T_2^* a maximum gate length (the dashed lines indicate $2N\tau = 5$ ms). For C_8, the many spins in close spectral proximity result in a lower attainable gate fidelity.

[Eq. (I5)] for ten magnetic fields uniformly sampled within $2\sigma_B$. To calculate the final fidelity, we compute an average weighted by the magnetic field probability distribution.

In typical experimental settings [14,21], rf spin-echo pulses are performed after the gate to counter nuclear-spin dephasing. We simulate this by explicitly correcting for additional phases acquired by the spins in the register due to the sampled magnetic field offsets. We update the calculated unitary according to

$$U_c' = R_z(-2N\tau\gamma_c\,\delta_B)U_c. \tag{I7}$$

To give further insight into the effect of each source of infidelity, we investigate their cumulative effects on the infidelity for C_4 (Fig. 9). We also present the gate-fidelity maps for all five electron-controlled gates in the six-qubit register (Fig. 10).

APPENDIX J: ANALYTICAL DESCRIPTION OF DDrf GATES

In this appendix, we present an exact analytical solution of the evolution during a DDrf gate, when rf driving is neglected when the electron is in $|0\rangle$. Although this approximation is only valid in the regime in which $\Delta > 1/\tau$, it provides considerable insight into the spin dynamics for the general $\Delta < 1/\tau$ case.

The electron-nuclear Hamiltonian, only considering driving the electron $|1\rangle$ state, in the rotating frame of the rf radiation, is given by

$$H_{\mathrm{rf},|1\rangle} = |0\rangle\langle 0| \otimes \Delta_0 I_z + |1\rangle\langle 1| \otimes (\Delta_1 I_z + \Omega(\cos\phi I_x + \sin\phi I_y)). \tag{J1}$$

The following derivation shows similarities to the derivation used to analyze resonant DD control of nuclear spins [12]. In this approximation of driving during only one electron state, there are two differences between DD and DDrf: the Rabi frequency Ω takes the role of $A_\perp$ in resonant DD, and the phase of the rf driving can be changed between pulses, while for DD $A_\perp$ always acts along the same axis in the laboratory frame.

The unitary operator $U_{\mathrm{N}=2}$ that describes the action of a single ($N = 2$) DDrf block is given by

$$U_{\mathrm{DDrf},N=2} = e^{-iH_{\mathrm{rf}}\tau}(R_x(\pi)\otimes R_z(\delta_\phi))e^{-2iH_{\mathrm{rf}}\tau}(R_x(\pi)\otimes R_z(\delta_\phi))e^{-iH_{\mathrm{rf}}\tau}, \tag{J2}$$

where the $R_z(\delta_\phi) = e^{-i\delta_\phi\sigma_z/2}$ are the phase jumps of the rf radiation in between pulses, represented as z rotations of the rotating frame of the nuclear-spin qubit, and the $R_x(\pi)$ are rotations of angle π around the x axis of the electron spin, representing the decoupling pulses.

Due to the block-diagonal nature of the driving Hamiltonian, we can define $e^{-iH_{\mathrm{rf}}\tau} = |0\rangle\langle 0| \otimes T_0 + |1\rangle\langle 1| \otimes T_1$, with the unitary operators T_i describing the nuclear-spin evolution if the electron spin is in state $|i\rangle$. A DDrf gate

with 2 decoupling pulses can then be written as

$$U_{\mathrm{DDrf},N=2} = -|0\rangle\langle 0| \otimes T_0 R_z(\delta_\phi) T_1^2 R_z(\delta_\phi) T_0 - |1\rangle\langle 1| \otimes T_1 R_z(\delta_\phi) T_0^2 R_z(\delta_\phi) T_1 \quad \text{(J3)}$$

$$= -|0\rangle\langle 0| \otimes V_0 - |1\rangle\langle 1| \otimes V_1, \quad \text{(J4)}$$

which is a form similar to that obtained for DD in Ref. [12]. Any DDrf gate with more pulses can be found from $(U_{\mathrm{DDrf},N=2})^{N/2}$. The operator V_0 (V_1) is the unitary evolution of the nuclear spin during one DDrf gate $N = 2$ unit cell, with the electron spin initially in $|0\rangle$ ($|1\rangle$).

Again analogous to Ref. [12], V_0 and V_1 can be interpreted as rotations of the nuclear spin under an angle $\theta_0 = \theta_1 = \theta$ and around axes $\hat{\mathbf{n}}_0$ and $\hat{\mathbf{n}}_1$: $V_i = e^{-i\theta/2\hat{\mathbf{n}}_i\cdot\vec{\sigma}}$, with $\vec{\sigma} = \{\sigma_x, \sigma_y, \sigma_z\}$. The rotation angle and the inner product of the rotation axes are given by

$$\cos\theta = \cos(\Omega_{\mathrm{rot}}\tau)\cos(\Delta_0\tau + \delta_\phi) - \frac{\Delta_1}{\Omega_{\mathrm{rot}}}\sin(\Omega_{\mathrm{rot}}\tau)\sin(\Delta_0\tau + \delta_\phi), \quad \text{(J5)}$$

$$1 - \hat{\mathbf{n}}_0\cdot\hat{\mathbf{n}}_1 = \frac{\Omega^2}{\Omega_{\mathrm{rot}}^2}\frac{(1-\cos(\Omega_{\mathrm{rot}}\tau))(1-\cos(\Delta_0\tau+\delta_\phi))}{1+\cos\theta}, \quad \text{(J6)}$$

where $\Omega_{\mathrm{rot}} = \sqrt{\Omega^2 + \Delta_1^2}$. For larger N, the solution is given by the same rotation axes but by a rotation angle $\Theta = N\theta/2$.

The key difference compared to the analytical result for DD gates is that the resonance condition for an entangling gate can be fulfilled by setting δ_ϕ appropriately, whereas for DD only the decoupling time τ is used. Tracking the nuclear-spin evolution by setting $\delta_\phi = -\Delta_0\tau + \pi$, we find that

$$\cos\theta = -\cos\Omega_{\mathrm{rot}}\tau, \quad \text{(J7)}$$

$$1 - \hat{\mathbf{n}}_0\cdot\hat{\mathbf{n}}_1 = \frac{2}{1+\Delta_1^2/\Omega^2}. \quad \text{(J8)}$$

A fully entangling gate (e.g., $\hat{\mathbf{n}}_0\cdot\hat{\mathbf{n}}_1 = -1, N\theta/2 = \pi/2$) can be performed when $\Delta_1 = 0, \Omega = \pi/2N\tau$.

Due to the $(S_z I_x)$ nature of the interaction, it is useful to consider an experiment in which the electron is prepared in $|x\rangle = \frac{1}{\sqrt{2}}(|0\rangle + |1\rangle)$ and a DDrf sequence is applied. With the nuclear spin in a mixed state, the probability that the electron spin will remain in the $|x\rangle$ state is given by $P_x = \langle S_x\rangle + \frac{1}{2}$, with [12]

$$\langle S_x\rangle = \frac{1}{2}\left(1 - (1 - \hat{\mathbf{n}}_0\cdot\hat{\mathbf{n}}_1)\sin^2\frac{N\theta}{2}\right), \quad \text{(J9)}$$

which, under the resonance condition $\delta_\phi = -\Delta_0\tau + \pi$, is equal to

$$\langle S_x\rangle = \frac{1}{2}\left(1 - \frac{2}{1+\Delta_1^2/\Omega^2}\sin^2\left(\frac{N\tau}{2}\sqrt{\Omega^2+\Delta_1^2}\right)\right). \quad \text{(J10)}$$

Alternatively, δ_ϕ can be set to optimally drive a target spin for $\Delta_1 \neq 0$, tracking its phase evolution during the gate. The solution is $\delta_\phi \approx -\Delta_1\tau - \Delta_0\tau + \pi$ [the same as Eq. (3); for a derivation, see Appendix K]. In this case, Eq. (J5) can be approximated in the limit of small rotations per rf pulse ($\Omega\tau \ll 1$), to yield

$$\cos\theta = -\left(1 - \frac{1}{2}(\Omega\tau\,\mathrm{sinc}(\Delta_1\tau))^2\right) + O\left(\Omega^4\tau^4\right), \quad \text{(J11)}$$

so that each $N = 2$ DDrf block induces a rotation of the nuclear spin by

$$\theta \approx \Omega\tau\,\mathrm{sinc}(\Delta_1\tau) + \pi. \quad \text{(J12)}$$

This matches the effective Rabi frequency in the main text [Eq. (5)], in the limit considered here, where the driving in the $|0\rangle$ state is neglected ($\Delta_0\tau \ll 1$), and demonstrates the rf pulse bandwidth due to τ. The more general case is derived in Appendix K.

APPENDIX K: EFFECTIVE-RABI-FREQUENCY DERIVATION

As additional justification for the equation for $\tilde{\Omega}$ [Eq. (5)], next to the experimental data in the main text, we present a derivation that shows that the DDrf gate can be approximated by a rotation with a reduced Rabi frequency.

The matrix exponentials T_0 and T_1, as defined in Appendix J, can be explicitly calculated:

$$T_0 = \cos(\tau\sqrt{\Delta_0^2+\Omega^2}/2)\mathbb{I} - i\Omega\tau/2\,\mathrm{sinc}\left(\tau\sqrt{\Delta_0^2+\Omega^2}/2\right)\sigma_x - i\Delta_0\tau/2\,\mathrm{sinc}\left(\tau\sqrt{\Delta_0^2+\Omega^2}/2\right)\sigma_z, \quad \text{(K1)}$$

$$T_1 = \cos(\tau\sqrt{\Delta_1^2+\Omega^2}/2)\mathbb{I} - i\Omega\tau/2\,\mathrm{sinc}\left(\tau\sqrt{\Delta_1^2+\Omega^2}/2\right)\sigma_x - i\Delta_1\tau/2\,\mathrm{sinc}\left(\tau\sqrt{\Delta_1^2+\Omega^2}/2\right)\sigma_z, \quad \text{(K2)}$$

where σ_x and σ_z are the Pauli spin matrices. This form allows an efficient and accurate numerical calculation of the unitary operator of the DDrf gate (as only

multiplication of 2×2 matrices is required), which has been used to calculate the individual spin signals in Figs. 2(b) and 5(d) (see Appendix C).

Directly calculating V_0 or V_1 results in an analytically complex expression that is not easily simplified. Progress can be made by considering the limit $\Omega\tau \ll 1$. This is justified, as DDrf is designed to target weakly coupled nuclear spins ($\Delta < 1/T^*_{2,e}$), for which decoupling of the electron spin is needed, breaking up the rotation of the nuclear spin into small amounts.

To first order in $\Omega\tau$, $U_{\mathrm{DDrf},N=2}$ [Eq. (J3)] can be approximated by

$$\begin{aligned}
V_0 = {} & \mathbb{I}\left[\cos(\tau(\Delta_0+\Delta_1)+\delta_\phi)+O\left(\Omega^2\tau^2\right)\right] \\
& - \sigma_x\left[\frac{i\Omega\tau(\Delta_1(\sin(\tau(\Delta_0+\Delta_1)+\delta_\phi)-\sin(\Delta_1\tau+\delta_\phi))+\Delta_0\sin(\Delta_1\tau))}{\Delta_0\Delta_1\tau}+O\left(\Omega^3\tau^3\right)\right] \\
& - \sigma_z\left[i\sin(\tau(\Delta_0+\Delta_1)+\delta_\phi)+O\left(\Omega^2\tau^2\right)\right], \\
V_1 = {} & \mathbb{I}\left[\cos(\tau(\Delta_0+\Delta_1)+\delta_\phi)+O\left(\Omega^2\tau^2\right)\right] \\
& - \sigma_x\left[\frac{i\Omega\tau(\Delta_0(\sin(\tau(\Delta_0+\Delta_1)+\delta_\phi)-\sin(\Delta_0\tau+\delta_\phi))+\Delta_1\sin(\Delta_0\tau))}{\Delta_0\Delta_1\tau}+O\left(\Omega^3\tau^3\right)\right] \\
& - \sigma_z\left[i\sin(\tau(\Delta_0+\Delta_1)+\delta_\phi)+O\left(\Omega^2\tau^2\right)\right].
\end{aligned}$$

Thus the action of the DDrf gate on the nuclear spin can be approximated by a z rotation, and by an x rotation by an angle that scales linearly with Ω, as would be expected. The derivation also shows the δ_ϕ resonance conditions. Setting $\delta_\phi = -\Delta_0\tau - \Delta_1\tau + \pi$ results in

$$V_{0,\mathrm{con}} = \mathbb{I} - \sigma_x i\Omega\tau(\mathrm{sinc}(\Delta_1\tau) - \mathrm{sinc}(\Delta_0\tau)) + O\left(\Omega^2\tau^2\right), \tag{K3}$$

$$V_{1,\mathrm{con}} = \mathbb{I} + \sigma_x i\Omega\tau(\mathrm{sinc}(\Delta_1\tau) - \mathrm{sinc}(\Delta_0\tau)) + O\left(\Omega^2\tau^2\right), \tag{K4}$$

which describes (to first order) an x rotation conditional on the electron state, with a modified Rabi frequency $\tilde{\Omega}$ described by Eq. (5).

Setting $\delta_\phi = -\Delta_0\tau - \Delta_1\tau$ results in the operators

$$\begin{aligned}
V_{0,\mathrm{uncon}} = V_{1,\mathrm{uncon}} = {} & \mathbb{I} - \sigma_x i\Omega\tau(\mathrm{sinc}(\Delta_0\tau) + \mathrm{sinc}(\Delta_1\tau)) \\
& + O\left(\Omega^2\tau^2\right),
\end{aligned} \tag{K5}$$

which describe an unconditional x rotation.

One higher-order effect neglected in this analysis is the ac Stark shift [36], quadratic in Ω^2, which can shift the resonant phase increment δ_ϕ (see also Appendix D). Furthermore, in the regime in which $\Omega \gg \Delta$, the nuclear spin is driven by the rf field regardless of the electron spin state and the conditionality of the interaction is no longer dependent on the set phase increment [Eq. (3)]. Instead, the nuclear eigenstates become dressed along the x axis and decoupling the electron results in a perturbation along the z axis (the magnitude of which scales with $A_\parallel$). This regime can also be used for spin-selective sensing and control and forms the basis for the recently developed AERIS protocol [47].

[1] I. Lovchinsky, A. O. Sushkov, E. Urbach, N. P. de Leon, S. Choi, K. De Greve, R. Evans, R. Gertner, E. Bersin, C. Muller, L. McGuinness, F. Jelezko, R. L. Walsworth, H. Park, and M. D. Lukin, Nuclear magnetic resonance detection and spectroscopy of single proteins using quantum logic, Science **351**, 836 (2016).

[2] M. Pompili, S. L. N. Hermans, S. Baier, H. K. C. Beukers, P. C. Humphreys, R. N. Schouten, R. F. L. Vermeulen, M. Tiggelman, L. dos Santos Martins, B. Dirkse, S. Wehner, and R. Hanson, Realization of a multinode quantum network of remote solid-state qubits, Science **372**, 259 (2021).

[3] M. H. Abobeih, J. Randall, C. E. Bradley, H. P. Bartling, M. A. Bakker, M. J. Degen, M. Markham, D. J. Twitchen, and T. H. Taminiau, Atomic-scale imaging of a 27-nuclear-spin cluster using a quantum sensor, Nature **576**, 411 (2019).

[4] J. Randall, C. E. Bradley, F. V. van der Gronden, A. Galicia, M. H. Abobeih, M. Markham, D. J. Twitchen, F. Machado, N. Y. Yao, and T. H. Taminiau, Many-body–localized discrete time crystal with a programmable spin-based quantum simulator, Science **374**, 1474 (2021).

[5] K. S. Cujia, K. Herb, J. Zopes, J. M. Abendroth, and C. L. Degen, Parallel detection and spatial mapping of large nuclear spin clusters, Nat. Commun. **13**, 1260 (2022).

[6] R. Budakian *et al.*, Roadmap on nanoscale magnetic resonance imaging, Nanotechnology **35**, 412001 (2024).

[7] G. L. Van De Stolpe, D. P. Kwiatkowski, C. E. Bradley, J. Randall, M. H. Abobeih, S. A. Breitweiser, L. C. Bassett, M. Markham, D. J. Twitchen, and T. H. Taminiau, Mapping a 50-spin-qubit network through correlated sensing, Nat. Commun. **15**, 2006 (2024).

[8] T. Xie, Z. Zhao, S. Xu, X. Kong, Z. Yang, M. Wang, Y. Wang, F. Shi, and J. Du, 99.92%-Fidelity CNOT gates in solids by noise filtering, Phys. Rev. Lett. **130**, 030601 (2023).

[9] H. P. Bartling, J. Yun, K. N. Schymik, M. van Riggelen, L. A. Enthoven, H. B. van Ommen, M. Babaie, F. Sebastiano, M. Markham, D. J. Twitchen, and T. H. Taminiau, Universal high-fidelity quantum gates for spin qubits in diamond, Phys. Rev. Appl. **23**, 034052 (2025).

[10] P. C. Humphreys, N. Kalb, J. P. J. Morits, R. N. Schouten, R. F. L. Vermeulen, D. J. Twitchen, M. Markham, and R. Hanson, Deterministic delivery of remote entanglement on a quantum network, Nature **558**, 268 (2018).

[11] S. L. N. Hermans, M. Pompili, H. K. C. Beukers, S. Baier, J. Borregaard, and R. Hanson, Qubit teleportation between non-neighbouring nodes in a quantum network, Nature **605**, 663 (2022).

[12] T. H. Taminiau, J. J. T. Wagenaar, T. van der Sar, F. Jelezko, V. V. Dobrovitski, and R. Hanson, Detection and control of individual nuclear spins using a weakly coupled electron spin, Phys. Rev. Lett. **109**, 137602 (2012).

[13] T. van der Sar, Z. H. Wang, M. S. Blok, H. Bernien, T. H. Taminiau, D. M. Toyli, D. A. Lidar, D. D. Awschalom, R. Hanson, and V. V. Dobrovitski, Decoherence-protected quantum gates for a hybrid solid-state spin register, Nature **484**, 82 (2012).

[14] C. E. Bradley, J. Randall, M. H. Abobeih, R. C. Berrevoets, M. J. Degen, M. A. Bakker, M. Markham, D. J. Twitchen, and T. H. Taminiau, A ten-qubit solid-state spin register with quantum memory up to one minute, Phys. Rev. X **9**, 031045 (2019).

[15] M. H. Abobeih, J. Cramer, M. A. Bakker, N. Kalb, M. Markham, D. J. Twitchen, and T. H. Taminiau, One-second coherence for a single electron spin coupled to a multi-qubit nuclear-spin environment, Nat. Commun. **9**, 2552 (2018).

[16] H. P. Bartling, M. H. Abobeih, B. Pingault, M. J. Degen, S. J. H. Loenen, C. E. Bradley, J. Randall, M. Markham, D. J. Twitchen, and T. H. Taminiau, Entanglement of spin-pair qubits with intrinsic dephasing times exceeding a minute, Phys. Rev. X **12**, 011048 (2022).

[17] I. Schwartz, J. Scheuer, B. Tratzmiller, S. Müller, Q. Chen, I. Dhand, Z.-Y. Wang, C. Müller, B. Naydenov, F. Jelezko, and M. B. Plenio, Robust optical polarization of nuclear spin baths using Hamiltonian engineering of nitrogen-vacancy center quantum dynamics, Sci. Adv. **4**, eaat8978 (2018).

[18] T. Staudacher, F. Shi, S. Pezzagna, J. Meijer, J. Du, C. A. Meriles, F. Reinhard, and J. Wrachtrup, Nuclear magnetic resonance spectroscopy on a (5-nanometer)^3 sample volume, Science **339**, 561 (2013).

[19] K. S. Cujia, J. M. Boss, K. Herb, J. Zopes, and C. L. Degen, Tracking the precession of single nuclear spins by weak measurements, Nature **571**, 230 (2019).

[20] T. H. Taminiau, J. Cramer, T. van der Sar, V. V. Dobrovitski, and R. Hanson, Universal control and error correction in multi-qubit spin registers in diamond, Nat. Nanotechnol. **9**, 171 (2014).

[21] M. H. Abobeih, Y. Wang, J. Randall, S. J. H. Loenen, C. E. Bradley, M. Markham, D. J. Twitchen, B. M. Terhal, and T. H. Taminiau, Fault-tolerant operation of a logical qubit in a diamond quantum processor, Nature **606**, 884 (2022).

[22] S. K. Parthasarathy, B. Kallinger, F. Kaiser, P. Berwian, D. B. Dasari, J. Friedrich, and R. Nagy, Scalable quantum memory nodes using nuclear spins in silicon carbide, Phys. Rev. Appl. **19**, 034026 (2023).

[23] C. Babin *et al.*, Fabrication and nanophotonic waveguide integration of silicon carbide colour centres with preserved spin-optical coherence, Nat. Mater. **21**, 67 (2022).

[24] M. T. Uysal, M. Raha, S. Chen, C. M. Phenicie, S. Ourari, M. Wang, C. G. Van De Walle, V. V. Dobrovitski, and J. D. Thompson, Coherent control of a nuclear spin via interactions with a rare-earth ion in the solid state, PRX Quantum **4**, 010323 (2023).

[25] D. B. Higginbottom *et al.*, Optical observation of single spins in silicon, Nature **607**, 266 (2022).

[26] R. Debroux, C. P. Michaels, C. M. Purser, N. Wan, M. E. Trusheim, J. Arjona Martínez, R. A. Parker, A. M. Stramma, K. C. Chen, L. de Santis, E. M. Alexeev, A. C. Ferrari, D. Englund, D. A. Gangloff, and M. Atatüre, Quantum control of the tin-vacancy spin qubit in diamond, Phys. Rev. X **11**, 041041 (2021).

[27] A. Sipahigil, R. E. Evans, D. D. Sukachev, M. J. Burek, J. Borregaard, M. K. Bhaskar, C. T. Nguyen, J. L. Pacheco, H. A. Atikian, C. Meuwly, R. M. Camacho, F. Jelezko, E. Bielejec, H. Park, and M. Lon, An integrated diamond nanophotonics platform for quantum-optical networks, Science **358**, 847 (2016).

[28] W.-R. Hannes, R. Finsterhoelzl, and G. Burkard, Fidelity of remotely entangled nuclear spin states in photon-connected multiqubit registers, Phys. Rev. A **110**, 052436 (2024).

[29] H. K. C. Beukers, C. Waas, M. Pasini, H. B. van Ommen, Z. Ademi, M. Iuliano, N. Codreanu, J. M. Brevoord, T. Turan, T. H. Taminiau, and R. Hanson, Control of solid-state nuclear spin qubits using an electron spin-1/2, Phys. Rev. X **15**, 021011 (2025).

[30] C. T. Nguyen, D. D. Sukachev, M. K. Bhaskar, B. Machielse, D. S. Levonian, E. N. Knall, P. Stroganov, R. Riedinger, H. Park, M. Lončar, and M. D. Lukin, Quantum network nodes based on diamond qubits with an efficient nanophotonic interface, Phys. Rev. Lett. **123**, 183602 (2019).

[31] M. Zahedian, V. Vorobyov, and J. Wrachtrup, Blueprint for efficient nuclear spin characterization with color centers, Phys. Rev. B **109**, 214111 (2024).

[32] I. Schwartz, J. Rosskopf, S. Schmitt, B. Tratzmiller, Q. Chen, L. P. McGuinness, F. Jelezko, and M. B. Plenio, Blueprint for nanoscale NMR, Sci. Rep. **9**, 6938 (2019).

[33] C. L. Degen, F. Reinhard, and P. Cappellaro, Quantum sensing, Rev. Mod. Phys. **89**, 035002 (2017).

[34] K. Herb, J. Zopes, K. S. Cujia, and C. L. Degen, Broadband radio-frequency transmitter for fast nuclear spin control, Rev. Sci. Instrum. **91**, 113106 (2020).

[35] D. Yudilevich, A. Salhov, I. Schaefer, K. Herb, A. Retzker, and A. Finkler, Coherent manipulation of nuclear spins in the strong driving regime, New J. Phys. **25**, 113042 (2023).

[36] L. M. K. Vandersypen and I. L. Chuang, NMR techniques for quantum control and computation, Rev. Mod. Phys. **76**, 1037 (2005).

[37] M. A. Nielsen, A simple formula for the average gate fidelity of a quantum dynamical operation, Phys. Lett. A **303**, 249 (2002).

[38] H. J. Mamin, M. Kim, M. H. Sherwood, C. T. Rettner, K. Ohno, D. D. Awschalom, and D. Rugar, Nanoscale nuclear magnetic resonance with a nitrogen-vacancy spin sensor, Science **339**, 557 (2013).

[39] C. E. Bradley, S. W. De Bone, P. F. W. Möller, S. Baier, M. J. Degen, S. J. H. Loenen, H. P. Bartling, M. Markham, D. J. Twitchen, R. Hanson, D. Elkouss, and T. H. Taminiau, Robust quantum-network memory based on spin qubits in isotopically engineered diamond, npj Quantum Inf. **8**, 122 (2022).

[40] S. De Bone, P. Möller, C. E. Bradley, T. H. Taminiau, and D. Elkouss, Thresholds for the distributed surface code in the presence of memory decoherence, AVS Quantum Sci. **6**, 033801 (2024).

[41] S. Singh, F. Gu, S. de Bone, E. Villaseñor, D. Elkouss, and J. Borregaard, Modular architectures and entanglement schemes for error-corrected distributed quantum computation, arXiv:2408.02837 [quant-ph].

[42] A. Bourassa, C. P. Anderson, K. C. Miao, M. Onizhuk, H. Ma, A. L. Crook, H. Abe, J. Ul-Hassan, T. Ohshima, N. T. Son, G. Galli, and D. D. Awschalom, Entanglement and control of single nuclear spins in isotopically engineered silicon carbide, Nat. Mater. **19**, 1319 (2020).

[43] B. Hensen, W. Wei Huang, C.-H. Yang, K. Wai Chan, J. Yoneda, T. Tanttu, F. E. Hudson, A. Laucht, K. M. Itoh, T. D. Ladd, A. Morello, and A. S. Dzurak, A silicon quantum-dot-coupled nuclear spin qubit, Nat. Nanotechnol. **15**, 13 (2020).

[44] A. Ruskuc, C.-J. Wu, J. Rochman, J. Choi, and A. Faraon, Nuclear spin-wave quantum register for a solid-state qubit, Nature **602**, 408 (2022).

[45] H. B. van Ommen, G. L. van de Stolpe, N. Demetriou, H. K. C. Beukers, J. Yun, T. R. J. Fortuin, M. Iuliano, A. R.-P. Montblanch, R. Hanson, and T. Taminiau, Data and simulations underlying the research article "Improved electron-nuclear quantum gates for spin sensing and control", https://data.4tu.nl/datasets/643ed69d-ced0-4d45-86b3-534a5b79c605

[46] L. Robledo, L. Childress, H. Bernien, B. Hensen, P. F. A. Alkemade, and R. Hanson, High-fidelity projective readout of a solid-state spin quantum register, Nature **477**, 574 (2011).

[47] C. Munuera-Javaloy, A. Tobalina, and J. Casanova, High-resolution NMR spectroscopy at large fields with nitrogen vacancy centers, Phys. Rev. Lett. **130**, 133603 (2023).